Polarization-Dependent Selection Rules and Optical Spectrum Atlas of Twisted Bilayer Graphene Quantum Dots

Yunhua Wang,[1,2,3,‡,*] Guodong Yu,[4,2,‡] Malte Rösner,[3] Mikhail I. Katsnelson,[3] Hai-Qing Lin,[1,5] and Shengjun Yuan[2,1,3,†]

[1]*Beijing Computational Science Research Center, Beijing 100193, China*
[2]*Key Laboratory of Artificial Micro-and Nano-structures of Ministry of Education and School of Physics and Technology, Wuhan University, Wuhan 430072, China*
[3]*Institute for Molecules and Materials, Radboud University, Heijendaalseweg 135, NL-6525 AJ Nijmegen, Netherlands*
[4]*Center for Quantum Sciences and School of Physics, Northeast Normal University, Changchun 130024, China*
[5]*School of Physics, Zhejiang University, Hangzhou 310027, China*

(Received 5 October 2021; revised 14 April 2022; accepted 3 May 2022; published 9 June 2022)

Understanding how symmetries encode optical polarization information into selection rules in molecules and materials is important for their optoelectronic applications including spectroscopic analysis, display technology, and quantum computation. Here, we extend polarization-dependent selection rules from atoms to solid-state systems with various point groups with the help of the rotational operator for circular polarization and the twofold rotational operator (or reflection operator) for linear polarization. We use these new selection rules to study the optical properties of twisted bilayer graphene quantum dots (TBGQDs), which inherit advantages of graphene quantum dot including its ultrathin thickness, excellent biocompatibility, and shape- and size-tunable optical absorption or emission. We study how the electronic structures and optical properties of TBGQDs rely on size, shape, twist angle, and correlation effects for TBGQDs with 10 different point groups for which we obtain an optical selection rule database. We show how current operator matrix elements identify the generalized polarization-dependent selection rules. Our results show that both the electronic and optical band gaps follow power-law size scalings with a dominant role of the twist angle. We derive an atlas of optical conductivity spectra for both size and twist angle in TBGQDs. As a result of quantum confinement effects, in the atlas a new type of optical conductivity features emerges with multiple discrete absorption frequencies ranging from infrared to ultraviolet energy, allowing for applications in photovoltaic devices and photodetectors. The atlas and size scaling provide a full structure–symmetry-function interrelation and hence offer an excellent basis for the geometrical manipulation of optical properties of TBGQDs as building blocks for novel integrated carbon optoelectronics.

DOI: 10.1103/PhysRevX.12.021055 Subject Areas: Graphene, Optoelectronics

I. INTRODUCTION

Optical polarization, i.e., the oscillating direction of the electric field, can be generated, controlled, and detected by means of the light-matter interaction, yielding various polarization-dependent phenomena, such as birefringence, dichroism, optical activity, Kerr effect, etc. As such, optical polarization effects are important for widespread applications including photodetectors [1], laser and display technologies, spectroscopic analysis [2], and quantum computation [3,4]. Optical selection rules specify possible transitions between energy levels via absorption or emission of electromagnetic radiation in various systems ranging from atoms to molecules and solids. These rules are essentially strict constraints resulting from both system symmetries and conservation laws, and hence are of vital importance for understanding the optical spectrum and for determining the system's symmetries and electronic properties. Besides the constraint from the angular momentum conservation, the selection rules of both circularly and linearly polarized light for hydrogen atoms in electric dipole approximation are described by the magnetic quantum number changes $\Delta m = \pm 1$ and $\Delta m = 0$ [5],

*wangyunhua@csrc.ac.cn
†s.yuan@whu.edu.cn
‡Y. W. and G. Y. contributed equally to this work.

respectively. For the past several years, it has also been indicated that, as a result of constraints from lattice and time-reversal symmetries, optical interband transitions for left- and right-handed circular polarizations in some special semiconductors can display quite different behaviors. In addition, polarization-dependent selection rules are deeply tied to the internal quantum degrees of freedom of Bloch electrons, such as the spin and valley contrasting optical selection rules for circularly polarized light in III-V bulk crystals [6] and two-dimensional hexagonal semiconductors [7–11]. Recently, numerical calculations of the current operator matrix elements in graphene quantum dots (GQDs) have shown anomalous distribution patterns with respect to the rotational symmetry operator [12] resulting from the selection rule of polarized light. A natural question is whether the spin and valley contrasting optical selection rules in crystals and the anomalous optical selection rules in quantum dots can be extended to a uniform expression of polarization-dependent selection rules. In addition, understanding how symmetries encode the polarization of light into the selection rule is important to analyze both polarization-dependent optical spectra and symmetries of the electronic structure in solid materials, which subsequently allow for their applications in optoelectronics. Motivated by these examples, we generalize and augment the following optical selection rules for both linear and circular polarizations in molecules and solids by a point group description. Our theory shows that the selection rules of circularly polarized light are characterized by the changes in the rotational quantum number. The selection rules of linearly polarized light in D_n, D_{nh}, D_{nd}, and C_{nv} symmetric systems can also be correspondingly characterized by a twofold rotational operator or reflection operator of systems.

Compared with bulk semiconductors, quantum dots, i.e., zero-dimensional nanocrystals, have remarkable size- and shape-tunable energy levels and absorption or emission spectra due to quantum confinement effects [13,14], enabling a wide range of optoelectronic devices [15–18], such as displays, solar cells, and light-emitting diodes. GQDs, i.e., graphene nanofragments, are ultrathin, have excellent biocompatibility, can be easily functionalized, show a good photostability, and have shape- and size-controllable optical absorption as well as photoluminescence characteristics. GQDs hence hold high promises for applications in optical sensing [19,20], bioimaging [19–21], photovoltaics [22–24], photodetectors [25], and light-emitting diodes [22–24]. Several synthetic strategies are known to fabricate GQDs from a few nanometers to several hundred nanometers [19–28]. Theoretical investigations based on tight-binding models clearly reveal that the optical absorption of GQDs is modulated by the edge type [29], size [30,31], shape [32], and electronic correlation effects [31,33,34]. In addition, group theory analysis shows that symmetries play a key role in optical selection rules in GQDs [32,34].

Recently, twisted bilayer graphene has drawn considerable attention in condensed matters owing to its exotic electronic structure [35–38], emergent correlated effects [39,40], and quasicrystalline order [41,42]. The optical absorption properties of infinite-size twisted bilayer graphene have been explored theoretically [43–46], based on the p_z-orbital based tight-binding model. The twist angle dependence of optical absorptions in infinite systems has also been experimentally investigated [47], highlighting the absorption peaks from interband transitions between energy levels near the van Hove singularities (i.e., logarithmic divergent singularity in the density of states). It is thus natural to further ask how the electronic structures and optical properties rely on size, shape, twist angle, edge structure, and correlation effects in twisted bilayer graphene quantum dots (TBGQDs). The chiral optical properties including circular dichroism and optical activity are analyzed in TBGQDs with a D_n point group symmetry (with $n = 2, 3, 6$) [48]. Plasmonic excitations are studied in twisted bilayer supercells [49]. The radius-dependent energy levels together with electron localizations [50], valley-dependent scattering [51], and generic behavior of energy bands at large twisting angles [52] are discussed in potential-induced TBGQDs, which refer to twisted bilayer graphene with a confining boundary in the form of site-dependent staggered potentials (i.e., sublattice asymmetry) [50,51] or combinations of staggered and electrostatic potentials [52].

Here, we present an extensive study of various TBGQD structures with 10 different point groups determined by twist angles, geometrical centers, and edge restrictions. Applying the orthogonality theorem, we derive the optical selection rules for all these structures and show that numerically calculated current operator matrix elements follow these generalized polarization-dependent selection rules. The electronic band gaps of these quantum dots show a power-law size scaling with exponents ranging from -2 to -1. As a consequence of the selection rules, the optical conductivity spectra exhibit three remarkable absorption characteristics: (i) a relatively strong absorption occurs around $1.5t_0 < \hbar\omega < 2t_0$ (with $t_0 = 2.8$ eV), which is associated with the interband transitions between these energy levels near the van Hove singularities of twisted bilayer graphene [43,47]; (ii) the optical band gap scaling also follows a power law but with its power index less than that of electronic band gap; and (iii) the finite-size quantum confinement effect yields a new type of optical conductivity features besides the previous three types of conductivity peaks in infinite twisted bilayer graphene. This new type of peaks with multiple discrete absorption frequencies ranging from infrared to ultraviolet energy

enables potential applications in photovoltaic devices and photodetectors.

II. POLARIZATION-DEPENDENT SELECTION RULES

The optical conductivity formula indicates that the allowed transitions are determined by the nonzero matrix elements of the current operator $\hat{j}_\alpha$ with $\alpha = x, y, z$, i.e.,

$$\langle\psi_k|\hat{j}_\alpha|\psi_l\rangle \neq 0, \tag{1}$$

where $|\psi_k\rangle$ and $|\psi_l\rangle$ are eigenstates of the system. These nonzero matrix elements can be identified using the orthogonality theorem. The reducible representation of $\hat{j}_\alpha|\psi_l\rangle$ is the direct product representation, $\Gamma_{\hat{j}_\alpha} \otimes \Gamma_l$, which is usually written as the direct sum form $\sum_\mu^\oplus a_\mu\Gamma_\mu$ with a_μ counting how often the irreducible representation Γ_μ appears. If the current operators $\hat{j}_x$, $\hat{j}_y$, and $\hat{j}_z$ have different irreducible representations, the selection rules for different linearly polarized light are naturally distinguishable. From point group character tables [53,54] we can conclude that (i) except C_i and cubic point groups, all the other point groups have different irreducible representations for z and (x, y), and (ii) except the nonaxial group and D_2, C_{2v}, and D_{2h} point groups, all the other point groups have the same irreducible representations for x and y, as listed in Table I. The irreducible representation of $\hat{j}_\alpha$ is the same as that of α. In addition, considering that many 2D materials and their quantum dot structures have noncubic point group symmetry, we mainly aim for theoretical descriptions governing the selection rules of polarized light for these point groups with the same irreducible representations of $\hat{j}_x$ and $\hat{j}_y$. In this respect, we need to search for some symmetry operators to differentiate $\Gamma_{\hat{j}_{x(y)}} \otimes \Gamma_l$ for linear polarization and $\Gamma_{\hat{j}_\pm} \otimes \Gamma_l$ for right (σ^+) and left (σ^-) circular polarizations with $\hat{j}_\pm = \hat{j}_x \pm i\hat{j}_y$.

For circularly polarized light, we choose the rotational symmetry operator $\hat{C}_n(\hat{R}_{2\pi/n})$ with an n-fold z axis such that an arbitrary eigenstate $|\psi_l\rangle$ of system with the same Γ_l is distinguished by the eigenvalues (i.e., rotational quantum number ϕ_l) of $\hat{C}_n$, as follows:

$$\hat{C}_n|\psi_l\rangle = e^{(i2\pi/n)\phi_l}|\psi_l\rangle, \tag{2}$$

with $\phi_l = 0, \ldots, n-1$. For an allowed transition $k \leftrightarrow l$, the matrix elements of the current operator $\hat{j}_\pm$ for circular polarizations take the form

$$\langle\psi_k|\hat{j}_\pm|\psi_l\rangle = e^{(i2\pi/n)(\phi_k-\phi_l)}\langle\psi_k|\hat{C}_n^\dagger\hat{j}_\pm\hat{C}_n|\psi_l\rangle. \tag{3}$$

In addition, $\hat{j}_\pm$ under the rotational transformation is given by

$$\hat{C}_n^\dagger\hat{j}_\pm\hat{C}_n = e^{\pm i2\pi/n}\hat{j}_\pm. \tag{4}$$

Substituting Eq. (4) into Eq. (3) and using Eq. (1), we obtain $\phi_k - \phi_l \pm 1 = np$ with an integer p. However, the constraint of $|\phi_k - \phi_l| \leq n-1$ for both left and right circular polarizations requires $p = 0$. Therefore, the selection rule of circularly polarized light reads

$$\triangle\phi = \phi_l - \phi_k = \pm 1. \tag{5}$$

Equation (5) indicates that the changes of the rotational quantum number characterize the absorption and emission of circularly polarized light in systems with rotational symmetry operator $\hat{C}_n$. The selection rule in Eq. (5) is thus not limited to quantum dots. From Eqs. (3)–(5), the selection rules of circularly polarized light from the current operator matrix element can also be written as $\langle\psi_k|\hat{j}_\pm|\psi_l\rangle = \delta_{\phi_l,\phi_k\pm1}\langle\psi_k|\hat{j}_\pm|\psi_l\rangle$, which agrees with the result obtained from the dipole operator [55].

For linearly polarized light, we also need to find a symmetry operator $\hat{O}$ to characterize its selection rule. The

TABLE I. Summary on irreducible representations for z, x, and y in point group character tables. The ✓ (✗) sign denotes the distinguishable (indistinguishable) irreducible representations between z in the second row and (x, y) in the third row, or between x and y inside (x, y). $\hat{C}_n(z)$ is the rotational operator, i.e., $\hat{R}_{2\pi/n}$. The symmetry operator $\hat{O}$ for linearly polarized light can be $\hat{C}_2$, $\hat{C}_2^{\prime(\prime\prime)}$, or $\hat{\sigma}_{v(d)}$, with corresponding n inside curly braces. For instance, $\{3,5\}:\hat{C}_2/\hat{\sigma}_v$ for D_{nh} represents $\hat{O} = \hat{C}_2$ or $\hat{\sigma}_v$ for D_{3h} and D_{5h} point groups.

	Nonaxial	C_n	D_n	C_{nv}	C_{nh}	D_{nh}	D_{nd}	S_n	Cubic	$C_{\infty v}$	$D_{\infty h}$
z	C_s (✓) $C_{1(i)}$ (✗)	✓	✓	✓	✓	✓	✓	✓	✗	✓	✓
(x, y)		✗	D_2 (✓) others (✗)	C_{2v} (✓) others (✗)	✗	D_{2h} (✓) others (✗)	✗	✗	✗	✗	✗
$\hat{C}_n(z)$		$\hat{R}_{2\pi/n}$	$\hat{R}_{2\pi/n}$	$\hat{R}_{2\pi/n}$	$\hat{R}_{2\pi/n}$	$\hat{R}_{2\pi/n}$	$\hat{R}_{2\pi/n}$	$\hat{R}_{2\pi/n}$		$\hat{R}_{2\pi/n}$	$\hat{R}_{2\pi/n}$
$\hat{O}$			$\{3,5\}:\hat{C}_2$ $\{4,6\}:\hat{C}_2^{\prime(\prime\prime)}$	$\{3,5\}:\hat{\sigma}_v$ $\{4,6\}:\hat{\sigma}_{v(d)}$		$\{3,5\}:\hat{C}_2/\hat{\sigma}_v$ $\{4,6,8\}:\hat{C}_2^{\prime(\prime\prime)}/\hat{\sigma}_{v(d)}$	$\{3,5\}:\hat{C}_2/\hat{\sigma}_d$ $\{2,4,6\}:\hat{C}_2^{\prime}/\hat{\sigma}_d$			$\infty\hat{\sigma}_v$	$\infty\hat{\sigma}_v\infty\hat{C}_2$

operator $\hat{O}$ should satisfy two conditions: (i) $[\hat{H}, \hat{O}] = 0$ yielding $\hat{O}|\psi_i\rangle = \gamma_i|\psi_i\rangle$ with eigenvalue γ_i, and (ii) $\hat{O}^\dagger \hat{j}_\alpha \hat{O} = q_\alpha \hat{j}_\alpha$ with $q_x \neq q_y$ allowing to distinguish $\hat{j}_x$ and $\hat{j}_y$. For an allowed transition $k \leftrightarrow l$ the matrix elements of the current operator $\hat{j}_\alpha$ for linear polarizations then read

$$\langle\psi_k|\hat{j}_\alpha|\psi_l\rangle = q_\alpha(\gamma_k^*)^{-1}(\gamma_l)^{-1}\langle\psi_k|\hat{j}_\alpha|\psi_l\rangle. \tag{6}$$

Substituting Eq. (1) into Eq. (6), we obtain

$$\gamma_k^*\gamma_l - q_\alpha = 0. \tag{7}$$

Equation (7) characterizes the absorption and emission of linearly polarized light under the basis functions of $\hat{O}$. The possible symmetry operators $\hat{O}$ for D_n, C_{nv}, D_{nh}, D_{nd}, $C_{\infty v}$, and $D_{\infty h}$ point groups are listed in Table I, where $\hat{O}$ is absent for C_n, C_{nh}, and S_n point groups.

Now we turn back to examine the polarization-dependent selection rules within the previously studied GQDs [12,32] and two-dimensional hexagonal semiconductors [7–11]. As an example we consider MoS_2 monolayers with the D_{3h} point group symmetry. Its conduction and valence band edges at the $K_{+/-}$ valleys are of dominant Mo d_{z^2} and $\{d_{x^2-y^2}, d_{xy}\}$ orbital characters, respectively. The rotational operator $\hat{C}_3(\hat{R}_{2\pi/3})$ in the bases of $[d_{x^2-y^2}, d_{xy}, d_{z^2}]$ has the following representation:

$$\hat{C}_3[d_{x^2-y^2}, d_{xy}, d_{z^2}] = [d_{x^2-y^2}, d_{xy}, d_{z^2}]\begin{bmatrix} -\frac{1}{2} & \frac{\sqrt{3}}{2} & 0 \\ -\frac{\sqrt{3}}{2} & -\frac{1}{2} & 0 \\ 0 & 0 & 1 \end{bmatrix}. \tag{8}$$

Using Eq. (8), we can classify band edges by the rotational quantum number ϕ_l, i.e.,

$$\begin{aligned} d_{\phi_l=0} &= d_{z^2}, \\ d_{\phi_l=1} &= \frac{1}{\sqrt{2}}(d_{x^2-y^2} + id_{xy}), \\ d_{\phi_l=2} &= \frac{1}{\sqrt{2}}(d_{x^2-y^2} - id_{xy}). \end{aligned} \tag{9}$$

On the other hand, we also need to consider the constraint $E_{n,K_+,s} \neq E_{n,K_-,s}$ with energy E from the broken inversion symmetry and the constraint $E_{n,K_+,s} = E_{n,K_-,-s}$ from the time-reversal symmetry with the spin s. Therefore, $d_{\phi_l=1}$ and $d_{\phi_l=2}$ orbitals related by the time-reversal operation must be located at K_+ and K_-, respectively, as shown in Fig. 1. The selection rule of circularly polarized light, $\triangle\phi = \pm 1$ in Eq. (5), reflects the valley-resolved optical absorption from the analysis of azimuthal quantum number change of Mo atoms [9–11]. For GQDs with C_{3v} and C_{6v} point group symmetries, our selection rules from Eq. (5) directly indicate the transitions from ϕ_l to $\phi_l - 1$ and $\phi_l + 1$ for the corresponding σ^+ and σ^- circularly polarized light, and hence agree well with previous numerical calculations [12,32].

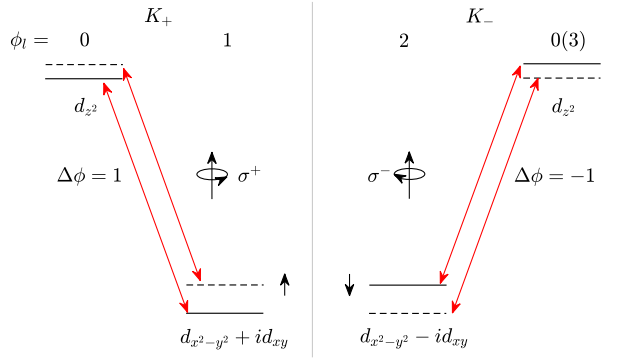

FIG. 1. The selection rule of circularly polarized light in MoS_2 monolayer. The conduction band bottom is mainly contributed by d_{z^2} orbital of Mo, and the top of valence band is mainly contributed by $\{d_{x^2-y^2}, d_{xy}\}$ orbitals of Mo. These band edges with spin-up (dash lines) and spin-down (solid lines) are classified by the rotational quantum number ϕ_l of $\hat{C}_3$ at K_+ (left) and K_- (right) valleys.

III. STRUCTURES OF TBGQDS

The combination of the twist degree of freedom, geometrical center positions, and edge restrictions results in a plethora of TBGQDs with various symmetries. Many of them can be categorized into 10 different point groups including D_{2h}, D_2, D_{3h}, D_3, C_{3v}, D_{3d}, D_{6h}, D_6, C_{6v}, and D_{6d}, as shown in Fig. 2. These structures with 10 different point group symmetries are generated following the procedures in the Appendix A. Their structural properties can be summarized as follows: (i) structures with D_{nh} point group are actually the *AA* stacked bilayer GQDs with a typical horizontal mirror plane, and structures with D_{3d} correspond to the *AB* stacked bilayer GQDs; (ii) geometrical centers are in the hexagon center for structures with other 7 point groups except D_2, D_{2h}, and D_{3d}, where the geometrical centers for D_2 and D_{2h} are at the middle of bond and at an atom for D_{3d}; (iii) the twist angles for C_{3v}, C_{6v}, and D_{6d} are $\pi/6$, and the twist angles for D_3 and D_6 can change from 0 to $\pi/6$ if the geometrical center is at the hexagon center and from 0 to $\pi/3$ if the geometrical center is at an atom, as a result of the twist periodicity; (iv) the x axes for D_{2h}, D_{3h}, and D_{6h} can be fixed along zigzag or armchair directions, and the x axes are chosen along $C_2(x)$ for D_2 and D_3, $\sigma_v(xz)$ for C_{3v}, D_{3h}, and C_{6v}, $\sigma_d(xz)$ for D_{3d} and D_{6d}, and $C_2'(x)$ for D_6 and D_{6h}.

All the irreducible representations, symmetry operators, and x axes of TBGQDs for the 10 different point groups are listed in Table S1 of Supplemental Material [56]. From this

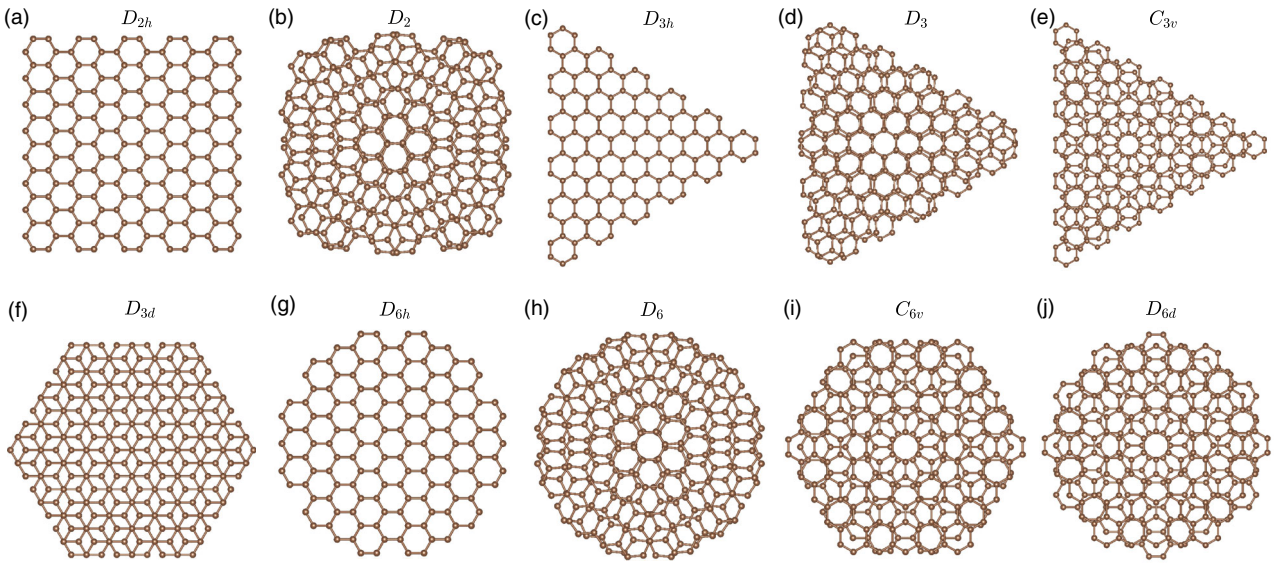

FIG. 2. Top views of TBGQDs with 10 different point group symmetries. Structures with D_{nh} have zero twist angle and hence the top layer covers vertically the bottom layer from top view in (a), (c), and (g) owing to the horizontal reflection σ_h. The structure with D_{3d} in (f) has the AB stacked configuration. In the sketched D_n structures the twist angles are chosen as 10° for D_2 in (b), 5° for D_3 in (d), and 10° for D_6 in (h). These structures with C_{3v} in (e), C_{6v} in (i), and D_{6d} in (j) have the fixed twist angle of 30°. All the symmetry operator elements and x axis for these 10 point groups are listed in Supplemental Material Table SI [56].

table we can summarize the following relations between these point groups.

(i) D_n and C_{nv} with $n = 3, 6$ have the same irreducible representations but slightly different symmetry operators, i.e., C_2, C_2', or C_2'' in D_n, and σ_v or σ_d in C_{nv},
(ii) $D_{nh} = D_n \otimes C_s$,
(iii) $D_{nd} = D_n \otimes C_i$.

Using the above relations we divide the 10 point groups into three sets of point group symmetries, i.e., set (1) $\{D_2, D_{2h}\}$, set (2) $\{D_3, C_{3v}, D_{3h}, D_{3d}\}$, and set (3) $\{D_6, C_{6v}, D_{6h}, D_{6d}\}$. Considering their geometrical edge profiles, we call sets (1) and (2) rectangular and triangular systems, respectively, and we further divide the set (3) into the hexagonal $\{D_6, C_{6v}, D_{6h}\}$ system and the dodecagonal $\{D_{6d}\}$ system.

IV. SELECTION RULES OF 10 POINT GROUPS

We apply the orthogonality theorem to derive the selection rules of the 10 point groups for TBGQDs. The direct product $\Gamma_{\hat{j}_\alpha} \otimes \Gamma_\mu$ for each irreducible representation Γ_μ and the selection rules of the 10 point groups are calculated and listed in Table II. From this table, we observe the following characteristics.

(i) D_n and C_{nv} with $n = 3, 6$ have the same selection rules, and the allowed transitions include $A_i \leftrightarrow E$ and $E \leftrightarrow E$.
(ii) Because of $D_{nh} = D_n \otimes C_s$ and $D_{nd} = D_n \otimes C_i$, D_{nh} and D_{nd} have close but different selection rules. For instance, for D_{3h} and D_{3d} the transitions are still only allowed between A and E states, or between E and E states, but there exist differences such as $E' \leftrightarrow E'$ for D_{3h} and $E_g \leftrightarrow E_u$ for D_{3d}.
(iii) For D_2 and D_{2h}, the selection rules for x and y polarized light are intrinsically different.

V. OPTICAL SPECTRUM

We now check the selection rules using the optical conductivity spectrum. The real part of optical conductivity corresponds to the interband absorption. The absorption peaks encode the information of the allowed transitions and hence manifest the selection rules. As an example, Fig. 3 shows the energy spectrum and optical conductivity spectrum of a D_{6d} point group structure with $N = 300$ atoms, where the Hamiltonian, irreducible representations, and optical conductivity are obtained following the approaches in Appendixes B, C, and D, respectively. We use the nearest-neighbor hopping energy t_0 as the energy unit and determine the Fermi energy E_F by the half filling rule. We can see a series of absorption peaks in Figs. 3(b) and 3(c) from infrared to ultraviolet frequencies, such as peak 1, $E_1 \to E_2$ at $\hbar\omega = 0.255t_0$; peak 2, $E_5 \to E_4$ at $\hbar\omega = 0.33t_0$; and peak 3, $A_1 \to E_1$ at $\hbar\omega = 0.485t_0$. In addition, the optical conductivity is obviously isotropic, i.e., $\sigma_{xx} = \sigma_{yy}$. Although the band gap with $E_g = 0.2t_0$ is determined by the energy difference between the highest occupied state E_1 and the lowest unoccupied state E_4 in Fig. 3(a), the transition $E_1 \leftrightarrow E_4$ is

TABLE II. Direct product $\Gamma_{j_\alpha} \otimes \Gamma_\mu$, selection rules, and symmetry operator $\hat{O}$ for TBGQDs. The 10 different point groups describe the corresponding symmetries of these structures in Fig. 2. For D_2 and D_{2h}, the selection rules for x and y polarized light are intrinsically distinguishable owing to the different irreducible representations of x and y. Here, $\hat{O}^\dagger \hat{j}_\alpha \hat{O} = q_\alpha \hat{j}_\alpha$ with $\alpha = x, y$, and $\hat{O}$ has been chosen such that $q_x = 1$ and $q_y = -1$ for all point groups.

Point groups	$\Gamma_{j_\alpha} \otimes \Gamma_\mu$	Selection rules	$\hat{O}$	q_x	q_y
D_3	$E \otimes A_1 = E, E \otimes A_2 = E$ $E \otimes E = A_1 \oplus A_2 \oplus E$	$A_1 \leftrightarrow E, A_2 \leftrightarrow E, E \leftrightarrow E$	$\hat{C}_2(x)$	$+1$	-1
D_{3h}	$E' \otimes A_1' = E', E' \otimes A_2' = E'$ $E' \otimes A_1'' = E'', E' \otimes A_2'' = E''$ $E' \otimes E' = A_1' \oplus A_2' \oplus E'$ $E'' \otimes E'' = A_1'' \oplus A_2'' \oplus E''$	$A_1' \leftrightarrow E', A_2' \leftrightarrow E', E' \leftrightarrow E'$ $A_1'' \leftrightarrow E'', A_2'' \leftrightarrow E'', E'' \leftrightarrow E''$	$\hat{\sigma}_v(xz)$	$+1$	-1
C_{3v}	$E \otimes A_1 = E, E \otimes A_2 = E$ $E \otimes E = A_1 \oplus A_2 \oplus E$	$A_1 \leftrightarrow E, A_2 \leftrightarrow E, E \leftrightarrow E$	$\hat{\sigma}_v(xz)$	$+1$	-1
D_{3d}	$E_u \otimes A_{1g} = E_u, E_u \otimes A_{2g} = E_u$ $E_u \otimes A_{1u} = E_g, E_u \otimes A_{2u} = E_g$ $E_u \otimes E_g = A_{1u} \oplus A_{2u} \oplus E_u$ $E_u \otimes E_u = A_{1g} \oplus A_{2g} \oplus E_g$	$A_{1g} \leftrightarrow E_u, A_{2g} \leftrightarrow E_u$ $A_{1u} \leftrightarrow E_g, A_{2u} \leftrightarrow E_g, E_g \leftrightarrow E_u$	$\hat{\sigma}_d(xz)$	$+1$	-1
D_6	$E_1 \otimes A_1 = E_1, E_1 \otimes A_2 = E_1$ $E_1 \otimes B_1 = E_2, E_1 \otimes B_2 = E_2$ $E_1 \otimes E_1 = A_1 \oplus A_2 \oplus E_2$ $E_1 \otimes E_2 = B_1 \oplus B_2 \oplus E_1$	$A_1 \leftrightarrow E_1, A_2 \leftrightarrow E_1$ $B_1 \leftrightarrow E_2, B_2 \leftrightarrow E_2, E_1 \leftrightarrow E_2$	$\hat{C}_2'(x)$	$+1$	-1
D_{6h}	$E_{1u} \otimes A_{1g} = E_{1u}, E_{1u} \otimes A_{2g} = E_{1u}$ $E_{1u} \otimes B_{1g} = E_{2u}, E_{1u} \otimes B_{2g} = E_{2u}$ $E_{1u} \otimes A_{1u} = E_{1g}, E_{1u} \otimes A_{2u} = E_{1g}$ $E_{1u} \otimes B_{1u} = E_{2g}, E_{1u} \otimes B_{2u} = E_{2g}$ $E_{1u} \otimes E_{1g} = A_{1u} \oplus A_{2u} \oplus E_{2u}$ $E_{1u} \otimes E_{2g} = B_{1u} \oplus B_{2u} \oplus E_{1u}$ $E_{1u} \otimes E_{1u} = A_{1g} \oplus A_{2g} \oplus E_{2g}$ $E_{1u} \otimes E_{2u} = B_{1g} \oplus B_{2g} \oplus E_{1g}$	$A_{1g} \leftrightarrow E_{1u}, A_{2g} \leftrightarrow E_{1u}$ $B_{1g} \leftrightarrow E_{2u}, B_{2g} \leftrightarrow E_{2u}$ $A_{1u} \leftrightarrow E_{1g}, A_{2u} \leftrightarrow E_{1g}$ $B_{1u} \leftrightarrow E_{2g}, B_{2u} \leftrightarrow E_{2g}$ $E_{1g} \leftrightarrow E_{2u}, E_{2g} \leftrightarrow E_{1u}$	$\hat{C}_2'(x)$	$+1$	-1
C_{6v}	$E_1 \otimes A_1 = E_1, E_1 \otimes A_2 = E_1$ $E_1 \otimes B_1 = E_2, E_1 \otimes B_2 = E_2$ $E_1 \otimes E_1 = A_1 \oplus A_2 \oplus E_2$ $E_1 \otimes E_2 = B_1 \oplus B_2 \oplus E_1$	$A_1 \leftrightarrow E_1, A_2 \leftrightarrow E_1$ $B_1 \leftrightarrow E_2, B_2 \leftrightarrow E_2, E_1 \leftrightarrow E_2$	$\hat{\sigma}_v(xz)$	$+1$	-1
D_{6d}	$E_1 \otimes A_1 = E_1, E_1 \otimes A_2 = E_1$ $E_1 \otimes B_1 = E_5, E_1 \otimes B_2 = E_5$ $E_1 \otimes E_1 = A_1 \oplus A_2 \oplus E_2$ $E_1 \otimes E_2 = E_1 \oplus E_3, E_1 \otimes E_3 = E_2 \oplus E_4$ $E_1 \otimes E_4 = E_3 \oplus E_5$ $E_1 \otimes E_5 = B_1 \oplus B_2 \oplus E_4$	$A_1 \leftrightarrow E_1, A_2 \leftrightarrow E_1$ $B_1 \leftrightarrow E_5, B_2 \leftrightarrow E_5$ $E_1 \leftrightarrow E_2, E_2 \leftrightarrow E_3$ $E_3 \leftrightarrow E_4, E_4 \leftrightarrow E_5$	$\hat{\sigma}_d(xz)$	$+1$	-1
D_2	$B_3 \otimes A = B_3, B_3 \otimes B_1 = B_2$ $B_3 \otimes B_2 = B_1, B_3 \otimes B_3 = A$ $B_2 \otimes A = B_2, B_2 \otimes B_1 = B_3$ $B_2 \otimes B_2 = A, B_2 \otimes B_3 = B_1$	x: $A \leftrightarrow B_3, B_1 \leftrightarrow B_2$ y: $A \leftrightarrow B_2, B_1 \leftrightarrow B_3$	$\hat{C}_2(x)$	$+1$	-1
D_{2h}	$B_{3u} \otimes A_g = B_{3u}, B_{3u} \otimes B_{1g} = B_{2u}$ $B_{3u} \otimes B_{2g} = B_{1u}, B_{3u} \otimes B_{3g} = A_u$ $B_{3u} \otimes A_u = B_{3g}, B_{3u} \otimes B_{1u} = B_{2g}$ $B_{3u} \otimes B_{2u} = B_{1g}, B_{3u} \otimes B_{3u} = A_g$ $B_{2u} \otimes A_g = B_{2u}, B_{2u} \otimes B_{1g} = B_{3u}$ $B_{2u} \otimes B_{2g} = A_u, B_{2u} \otimes B_{3g} = B_{1u}$ $B_{2u} \otimes A_u = B_{2g}, B_{2u} \otimes B_{1u} = B_{3g}$ $B_{2u} \otimes B_{2u} = A_g, B_{2u} \otimes B_{3u} = B_{1g}$	x: $A_g \leftrightarrow B_{3u}, B_{1g} \leftrightarrow B_{2u}$ $B_{2g} \leftrightarrow B_{1u}, B_{3g} \leftrightarrow A_u$ y: $A_g \leftrightarrow B_{2u}, B_{1g} \leftrightarrow B_{3u}$ $B_{2g} \leftrightarrow A_u, B_{3g} \leftrightarrow B_{1u}$	$\hat{C}_2(x)$	$+1$	-1

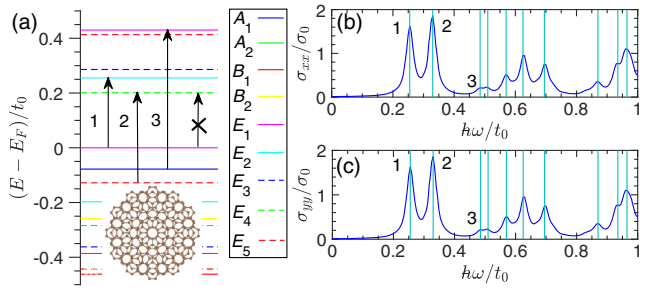

FIG. 3. Energy spectrum and optical conductivity spectrum of a D_{6d} TBGQD. (a) Energy spectrum with its irreducible representations, where the inset shows the structure with $N = 300$ atoms. The real part of optical conductivity as a function of photon energy $\hbar\omega/t_0$: σ_{xx} in (b) and σ_{yy} in (c) in unit of $\sigma_0 = \pi e^2/(4\hbar)$. Peaks 1, 2, and 3 in (b) and (c) arise from the corresponding transitions in (a). The transition $E_1 \leftrightarrow E_4$ is forbidden as a result of the selection rules in Table II.

forbidden. These absorption peaks and forbidden transitions are a result of the selection rules of D_{6d} point group as shown in Table II. The optical conductivity spectrum for the other 9 point group structures are also calculated and shown in Figs. S1–S3 of Supplemental Material [56] with the corresponding absorption peaks following the selection rules as well.

VI. MATRIX ELEMENTS OF CURRENT OPERATORS

To further understand how the allowed transitions for both linearly and circularly polarized light are identified by the symmetry operators $\hat{O}$ and $\hat{C}_n$, respectively, we first classify the energy levels via γ_l of $\hat{O}$ and ϕ_l of $\hat{C}_n$, as shown in Fig. 4, where $\hat{O} = \hat{\sigma}_d(xz)$ with the reflection plane xz and $\hat{C}_n = \hat{C}_6(z)$. As we can see, under the reflection operator $\hat{\sigma}_d$ in Fig. 4(b), the original energy levels in Fig. 4(c) are divided into two columns of energy levels denoted by $\gamma_l = 1$ and $\gamma_l = -1$ in Fig. 4(a). Under the rotational operator $\hat{C}_6(z)$ in Fig. 4(d), the original energy levels in Fig. 4(c) are separated into 6 columns of energy levels denoted by $\phi_l = 0$, 1, 2, 3, 4, 5 in Fig. 4(e). For linearly polarized light, $\hat{j}_x$ and $\hat{j}_y$ under the transformation of $\hat{\sigma}_d$ satisfy $\hat{\sigma}_d^\dagger \hat{j}_x \hat{\sigma}_d = \hat{j}_x$ and $\hat{\sigma}_d^\dagger \hat{j}_y \hat{\sigma}_d = -\hat{j}_y$. This means that $q_x = 1$ and $q_y = -1$. Therefore, the selection rules in Eq. (7) require that $\gamma_k^* \gamma_l - 1 = 0$ and $\gamma_k^* \gamma_l + 1 = 0$ for x and y linearly polarized light, respectively. Consequently, the calculated matrix elements of the current operators $\langle\psi_k|\hat{j}_x|\psi_l\rangle$ and $\langle\psi_k|\hat{j}_y|\psi_l\rangle$ have off-diagonal and diagonal patterns within the classified states of $\hat{\sigma}_d$, as illustrated in Figs. 4(f) and 4(g). Similarly, for right and left circularly polarized light, $\langle\psi_k|\hat{j}_+|\psi_l\rangle$ and $\langle\psi_k|\hat{j}_-|\psi_l\rangle$ within the classified states of $\hat{C}_6(z)$ correspondingly obey $\Delta\phi = 1$

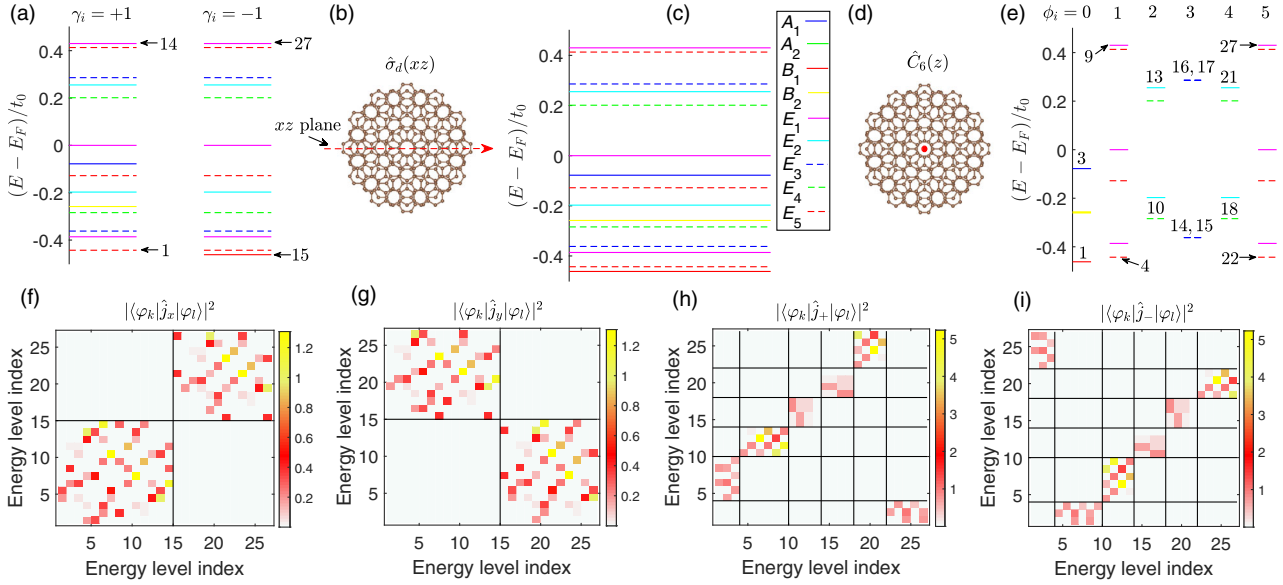

FIG. 4. Energy spectra and matrix elements of current operators for a D_{6d} TBGQD. Top view of the D_{6d} structure with $N = 300$ atoms is shown in (b) and (d), where the xz reflection plane and the z axis are represented by the red dashed line and the middle red dot, respectively. The pristine energy spectrum of the structure is plotted in (c). The classified energy spectra by γ_i of $\hat{\sigma}_d(xz)$ are shown in (a). The classified energy spectra by ϕ_i of $\hat{C}_6(z)$ are shown in (e). These energy levels from down to up are labeled by the increasing numbers for each γ_i and ϕ_i. The square modulus of current operator matrix elements in unit of t_0^2: $|\langle\psi_k|\hat{j}_x|\psi_l\rangle|^2$ in (f) and $|\langle\psi_k|\hat{j}_y|\psi_l\rangle|^2$ in (g) for linearly polarized light, and $|\langle\psi_k|\hat{j}_+|\psi_l\rangle|^2$ in (h) and $\langle|\psi_k|\hat{j}_-|\psi_l\rangle|^2$ in (i) for circularly polarized light. The energy level indexes in (f)–(i) represent these energy levels with the corresponding numbers in (a) and (e).

and $\Delta\phi = -1$ in Eq. (5), as demonstrated in Figs. 4(h) and 4(i). Since D_2 and D_{2h} have intrinsically anisotropic properties, we calculate these matrix elements of the current operators for structures with the other 7 point group symmetries and find similar results (see Figs. S4–S10 in Supplemental Material [56]) governed by the polarization-dependent selection rules in Eqs. (5) and (7).

VII. BAND GAP SCALING

The size dependence of the band gap is crucial for the practical designing and engineering of TBGQDs-based nanoelectronics. The area A of TBGQDs is written as $A = NA_0$, where N is the total number of C atoms and $A_0 = 3\sqrt{3}b_0^2/4$ is the average area per atom with $b_0 = 1.42$ Å as the bond length. Because the length scale L can be expressed by $L = \sqrt{A/2} \sim 0.1144\sqrt{N}$ nm with the factor 2 from two monolayers, the size (such as the edge length or radius) of TBGQDs is proportional to $\sqrt{N}$, and hence it is reasonable to use $\sqrt{N}$ as the size index.

Figure 5 presents the band gap of TBGQDs as a function of $\sqrt{N}$, for D_{3h}, $D_3(\theta = 1.1°)$, $D_3(\theta = 5°)$, $D_3(\theta = 10°)$, D_{6h}, $D_6(\theta = 5°)$, $C_{6v}(\theta = 30°)$, $D_{6d}(\theta = 30°)$, D_{2h}, and $D_2(\theta = 1.1°)$ point groups. We first discuss the common characteristic of the size-dependent band gap for these structures. As we can see in Fig. 5, the band gap exhibits firstly a rapid decay with respect to $\sqrt{N}$ from few hundreds to several thousands of N, and then converges with a possible oscillation toward zero because TBGQDs recover the electronic spectrum of twisted bilayer graphene with zero gap in the limit of large N. For usual semiconductor quantum dots, the band gap follows $1/R^2$ power law with the radius R [57]. For graphene ribbons, the scaling law obeys approximately $1/W$ (i.e., $1/\sqrt{N}$) and $1/W^2$ (i.e., $1/N$) relations with the ribbon width W for zigzag and armchair edges, respectively, because of their corresponding linear and parabolic energy dispersions [58]. Therefore, a power law of $E_g/t_0 = a(\sqrt{N})^b$ is adopted to fit the decay of the band gap of TBGQDs. These fitted values of the dimensionless numbers a and b are listed in Table III. All the values of the power index b are almost inside $[-2, -1]$, because our TBGQDs are generally customized with a random edge profile instead of pure zigzag or armchair edges such that the band gap scaling behaves like a mixed behavior of relativistic and nonrelativistic particles. In twisted bilayer graphene with a circular mass potential barrier, the band edge also exhibits a power-law scaling with the barrier radius [50].

We also discuss the twist angle dependence of the band gap scaling. For triangular systems in Figs. 5(a)–5(d), the absolute value of the power index b starts with a number close to 2 in D_{3h} structures and D_3 structures with a small twist angle, and then has an obvious decrease with the increasing angle [at 5° in Fig. 5(c)], and then increases back to the value about 2 with the further growth of the twist angle [at 10° in Fig. 5(d)]. A similar angle dependence of b exists for hexagonal systems in Figs. 5(e)–5(g). The band gap of the dodecagonal D_{6d} system in Fig. 5(h) has a very similar size dependence to that of the C_{6v} system in Fig. 5(g) owing to their similar structures. D_{2h} and $D_2(\theta = 1.1°)$ rectangular systems in Figs. 5(i) and 5(j) have slightly different values of b, but both values of $|b|$ are

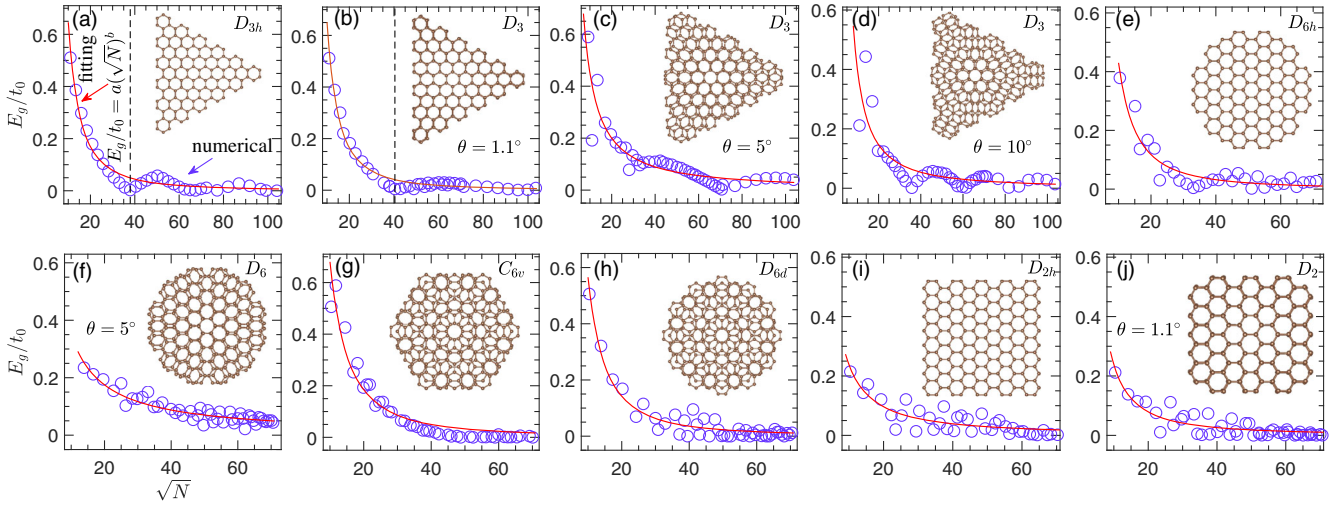

FIG. 5. Band gap scaling law of TBGQDs. From (a) to (j), each inset as an example shows the structure of quantum dot with its point group. Numerical results of E_g/t_0 as a function of $\sqrt{N}$ are denoted by the blue circles, and the power-law fitting of $E_g/t_0 = a(\sqrt{N})^b$ is plotted by the red line. All individual panels have the same labels of x and y axes, as labeled in (f). The fitted values of a and b are listed in Table III. In (a) and (b), the vertical dashed lines are respectively at $N = 1440$ and $N = 1632$, where the band gap of the structures vanishes.

TABLE III. Fitted values of dimensionless a and b for $U = 0$, $0.6t_0$, and $1.2t_0$.

		$U = 0$		$U = 0.6t_0$		$U = 1.2t_0$	
Point groups	Twist angle (θ)	a	b	a	b	a	b
D_{3h}	0°	54.889	−1.942	54.403	−1.926	53.652	−1.920
D_3	1.1°	62.217	−1.980	61.911	−1.978	61.477	−1.975
D_3	5°	14.894	−1.395	15.410	−1.408	15.651	−1.413
D_3	10°	95.092	−2.103	96.872	−2.110	95.553	−2.104
D_{6h}	0°	32.637	−1.879	32.640	−1.879	30.506	−1.851
D_6	5°	3.500	−0.995	3.430	−0.988	3.429	−0.988
C_{6v}	30°	52.096	−1.884	37.178	−1.749	19.987	−1.501
D_{6d}	30°	55.373	−1.991	49.765	−1.947	23.831	−1.645
D_{2h}	0°	4.832	−1.307	5.084	−1.329	7.142	−1.464
D_2	1.1°	9.399	−1.595	7.805	−1.521	10.513	−1.644

obviously less than those of D_{3h} and D_{6h}, as a consequence of the rectangular geometrical confinement.

In Fig. 5, our calculations only include the effective kinetic energy in the Hamiltonian in Eq. (B1). We further investigate the effects of local Coulomb interaction on the band gap scaling of TBGQDs. An effective on-site Coulomb repulsion U^* (here labeled as U) is adopted to capture the nonlocal Coulomb interactions [59]. The band gaps as a function of $\sqrt{N}$ for TBGQDs with $U = 1.2t_0$ [59,60] and $U = 0.6t_0$ are calculated and plotted in Figs. S11 and S12 in Supplemental Material [56], respectively. The variations in U are used to mimic the external environmental screening, e.g., $U = 0.6t_0$ from SiO_2 substrate with an effective dielectric constant κ^* about 2 [61]. As a consequence of Coulomb interactions, edge magnetism can emerge in some structures even with random edge profiles. The ground states are determined by minimizing the energy of ferromagnetic, antiferromagnetic, and nonmagnetic states. From the power-law fitting we obtain again the dimensionless numbers a and b also listed in Table III for comparison with the results under $U = 0$. As we can see, the local Coulomb interaction U has a weak influence on a and b for the structures with a fixed point group. This means that the effective tight-binding kinetic energy term of the Hamiltonian in Eq. (B1) can approximately capture the main scaling behaviors. Compared with the weak influence of the Coulomb interaction, the twist angle has a remarkable impact on the band gap scaling. Here we note that (i) quantum dots with odd number of C atoms such as C_{3v} structures are not discussed because of their zero band gap according to the half filling and (ii) small structures with several tens of C atoms are not discussed here because of the enhanced confinement effects, for which configuration interaction methods [62] and quantum Monte Carlo simulations [63] are alternative methods describing the correlation phenomena.

VIII. OPTICAL SPECTRUM ATLAS AND OPTICAL BAND GAP SCALING

Figure 6 shows an atlas of optical conductivity spectra as a function of the size index $\sqrt{N}$ and the photon energy $\hbar\omega$ for the same TBGQDs structures in each panel of Fig. 5. From Fig. 6 we can see two remarkable absorption characteristics. Firstly, at about $1.5t_0 < \hbar\omega < 2t_0$, there exists a relatively strong absorption region which changes only slightly with the system size for all structures (also see the line plots of the optical conductivity in Supplemental Material Fig. S13 [56]). Such a stable absorption region is related to the interband transitions between the energy levels near the van Hove singularities [43] of the infinite-size twisted bilayer graphene. Secondly, the forbidden absorption region below the fitted black dashed line vanishes with the increasing system size. Following the decay of the electronic band gap, the optical band gap ($\hbar\omega_g$) thus also decreases with the increasing system size. However, the fitting results in Table IV from the power law of $\hbar\omega_g/t_0 = c(\sqrt{N})^d$ show that the dimensionless numbers c and d are different from a and b of the electronic band gap. This arises from the interband transitions between the highest occupied and lowest unoccupied energy levels, which are only allowed if their transitions obey the optical selection rules in Table II. In addition, two further aspects are worth highlighting: (i) the D_{2h} and D_2 point group structures exhibit an anisotropic scaling behavior (see σ_{yy} in Supplemental Material Fig. S14 [56]), and (ii) the optical spectra of the D_{3h} and D_3 point group structures in Figs. 6(a) and 6(b) show a piecewise decay of the optical band gap as a result of the oscillating behavior of the electronic band gap [cf. Figs. 5(a) and 5(b)], with the vanishing band gaps at $N = 1440$ and $N = 1632$ (denoted by vertical dash lines), respectively. We plot the atlas of optical conductivity spectra for $U = 0.6t_0$ and $1.2t_0$ in Supplemental Material Figs. S15 and S16 [56], respectively, and we also list the fitting values of c and d in

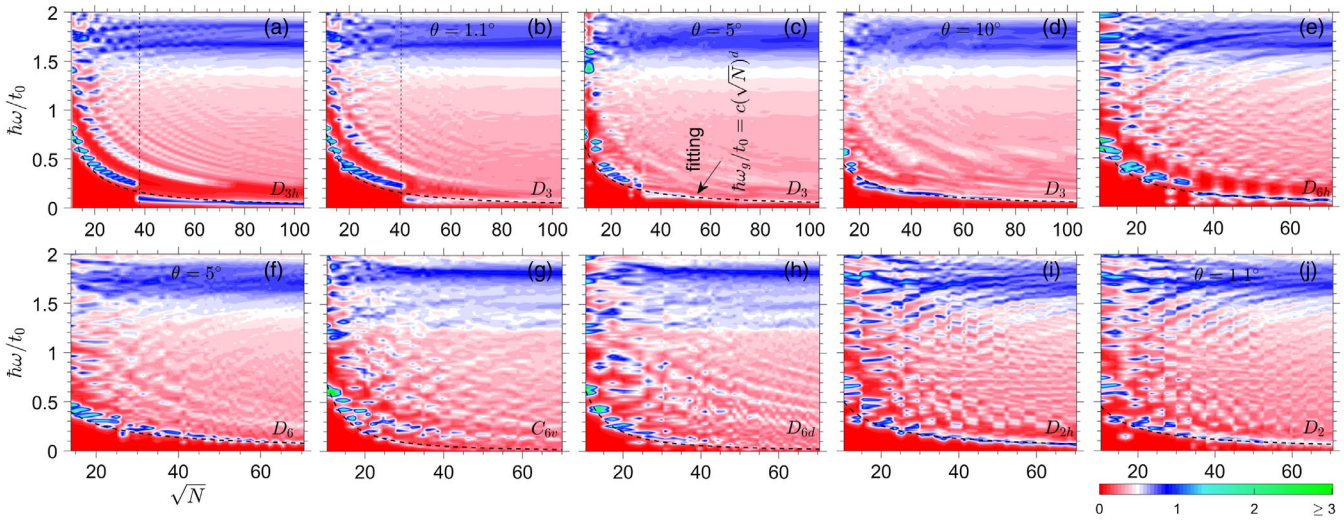

FIG. 6. Optical conductivity contour plots for $U = 0$. The real part of optical conductivity σ_{xx} in unit of $\sigma_0 = \pi e^2/(4\hbar)$ is plotted as a function of $\sqrt{N}$ and $\hbar\omega/t_0$ in (a)–(j) with the labeled point groups of TBGQDs. All individual panels have the same labels of x and y axes, as labeled in (f), and the color bar for all panels is at the bottom right-hand corner. The black dashed line represents the power-law fitting of $\hbar\omega_g/t_0 = c(\sqrt{N})^d$, with ω_g as the frequency of the first main absorption peak. The fitted values of c and d are listed in Table IV. In (a) and (b), the vertical dashed lines are respectively at $N = 1440$ and $N = 1632$, where the electronic band gap of the structures vanishes.

Table IV. As we can see, the effective Coulomb interaction has only weak influences on both the optical conductivity spectrum and the optical band gap scaling.

IX. STRUCTURE RELAXATIONS, EDGE ATOM VACANCIES, AND TWIST ANGLE EFFECTS ON OPTICAL SPECTRUM

We turn our focus now to the effects of structure relaxations (see Appendix E) and edge atom vacancies on the optical conductivity spectrum of TBGQDs. As shown in Supplemental Material Fig. S17 [56], the structure relaxation yields only weak modifications to the frequency and magnitude of the absorption features. As an example, Fig. 7 shows the optical conductivity spectrum of quantum dots with D_{2h}, D_2, C_{6v}, and D_{6d} point groups and different vacancy defect densities ρ (i.e., percentage of missing edge atoms). With the increasing ρ, the disorder is enhanced, and the original point group symmetry is broken, which damps the absorption peaks. Furthermore, we can see that (i) for low frequencies some new absorption peaks appear, as indicated by the arrows in Figs. 7(b)–7(d), and (ii) for high frequencies $(1.5 < \hbar\omega/t_0 < 2)$ the optical absorption associated with the van Hove singularity is only mildly affected.

Next, we evaluate the twist angle dependence of the optical absorption spectrum of TBGQDs with slightly variable N, which is inevitably induced in experiments due

TABLE IV. Fitted values of scaling indexes c and d for $U = 0$, $0.6t_0$, and $1.2t_0$.

		$U = 0$		$U = 0.6t_0$		$U = 1.2t_0$	
Point groups	Twist angle (θ)	c	d	c	d	c	d
D_{3h}	0°	16.477	−1.272	16.373	−1.270	16.373	−1.270
D_3	1.1°	14.199	−1.221	14.529	−1.229	15.443	−1.254
D_3	5°	14.699	−1.258	15.113	−1.268	15.063	−1.267
D_3	10°	10.182	−1.142	10.630	−1.158	10.350	−1.147
D_{6h}	0°	12.462	−1.247	12.462	−1.247	14.428	−1.314
D_6	5°	5.385	−0.994	5.443	−0.987	5.443	−0.987
C_{6v}	30°	57.320	−1.896	23.456	−1.545	15.717	−1.385
D_{6d}	30°	36.626	−1.745	25.501	−1.599	12.850	−1.325
$D_{2h}(x)$	0°	5.459	−1.022	5.459	−1.022	5.353	−1.015
$D_{2h}(y)$	0°	1.728	−0.788	1.728	−0.788	1.727	−0.784
$D_2(x)$	1.1°	4.935	−1.021	4.516	−0.988	4.466	−0.980
$D_2(y)$	1.1°	1.901	−0.839	1.825	−0.820	1.524	−0.756

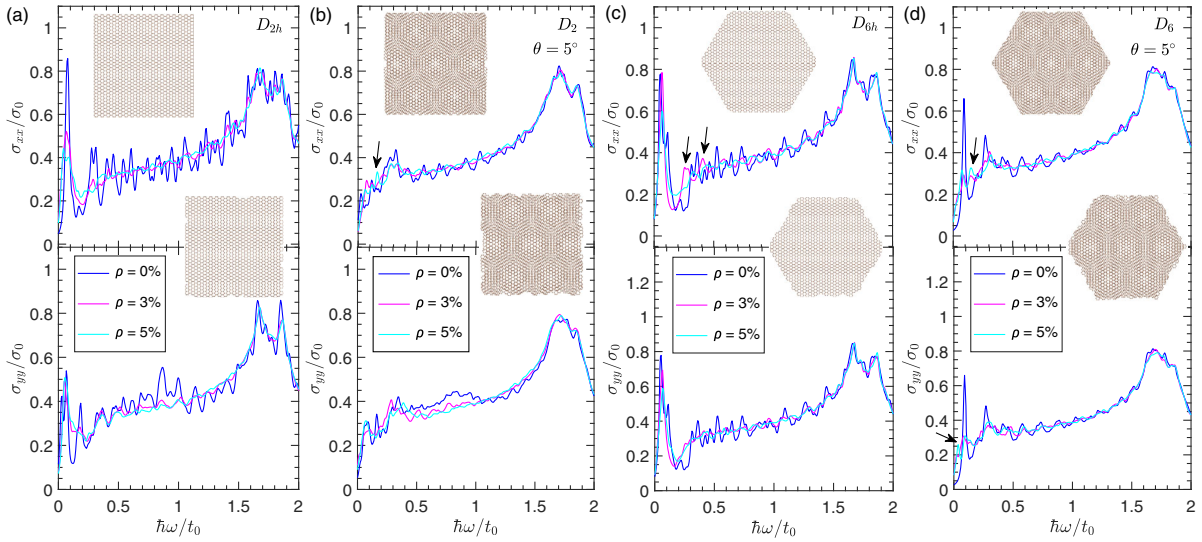

FIG. 7. Edge atom vacancy effects on optical conductivity spectrum. The real parts of optical conductivity σ_{xx} (upper panel) and σ_{yy} (lower panel) in unit of $\sigma_0 = \pi e^2/(4\hbar)$ are plotted as a function of $\hbar\omega/t_0$ with different vacancy densities ρ for D_{2h} in (a), D_2 in (b), D_{6h} in (c), and D_{6h} in (d). The upper (lower) insets show the quantum dot structures without (with) random edge atom vacancies. Here, $N = 4148$, $N = 4264$, $N = 4212$, and $N = 4344$ for these structures without vacancies in the upper insets from (a) to (d), respectively.

to the edge atom vacancies. We first consider a typically triangular quantum dot with a hexagon center and the x axis oriented along the armchair direction. The optical conductivities of the structures with $L \sim 3.54$ nm ($N \sim 955$) and $L \sim 8.03$ nm ($N \sim 4925$) are shown in Fig. 8 as a function of the twist angle θ and the photon energy $\hbar\omega$. For a relatively small structure with $N \sim 955$, we find three absorption peaks inside about $0.2t_0 < \hbar\omega < 0.7t_0$, i.e., in the infrared to visible frequency range, which vary only slightly for $\theta > 10°$ [cf. Fig. 8(b)]. For smaller angles $\theta < 10°$, these peaks split into several absorption regions, which shift with θ. For $\hbar\omega$ near $1.7t_0$ we see a broad absorption region, which can be associated with the transitions between the energy levels near the van Hove singularities. For a relatively large structure with $N \sim 4925$, we observe four groups of characteristic conductivity peaks, as indicated in Fig. 8(c). With the increasing twist angle, group (i) peaks shift toward higher frequencies, group (ii) peaks shift toward lower frequencies, and group (iii) peaks vary only slightly. The three groups of absorption peaks are associated with the van Hove singularity and behave similarly as those in the infinite-size twisted bilayer graphene [43]. Additionally, there exist the fourth group (iv) peaks with multiple discrete absorption frequencies ranging from infrared to ultraviolet energy, which are nearly independent of the twist angle above the angles of peaks (i). These peaks are missing in the infinite systems and arise from the multiple interband transitions between the discrete energy levels induced by the quantum confinement effects in finite-size systems. In addition, the group (iv) peaks also exist in other structures (see hexagonal quantum dots in Supplemental Material Fig. S18 [56]). Therefore, these

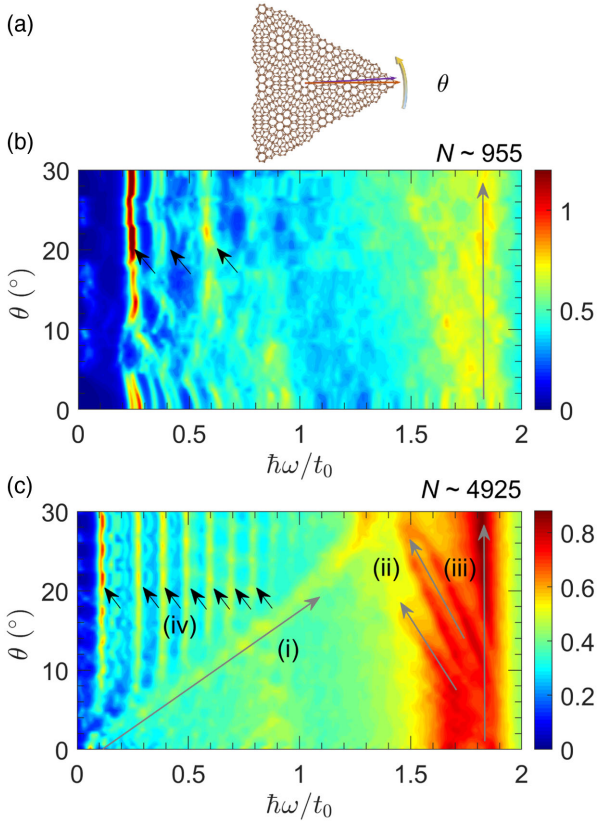

FIG. 8. Twist angle dependence of optical spectrum. (a) A schematic structure of a triangular quantum dot with the hexagon center and the fixed x axis along the armchair direction before the rotation. The real parts of optical conductivities σ_{xx} in unit of $\sigma_0 = \pi e^2/(4\hbar)$ are plotted as a function of the twist angle θ and the photon energy $\hbar\omega/t_0$ in (b) with $N \sim 955$ and in (c) with $N \sim 4925$.

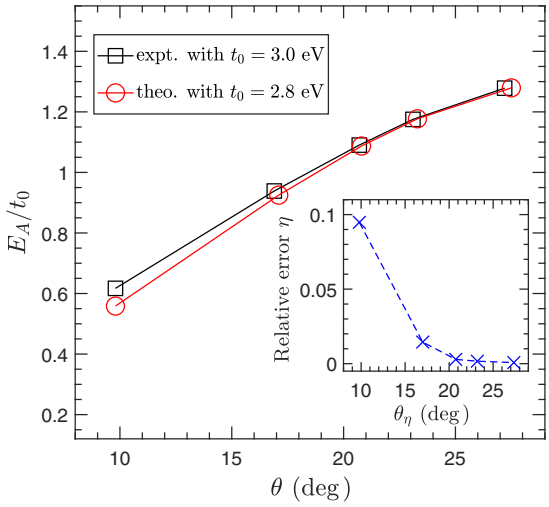

FIG. 9. A comparison of E_A/t_0 between experiment (expt.) and theory (theo.). The experimental energy positions of absorption peaks E_A at $\theta = 9.8°$, $\theta = 16.9°$, $\theta = 20.7°$, $\theta = 23.1°$, and $\theta = 27.2°$ are extracted from Fig. 3(a) in Ref. [47]. The theoretical energy positions of E_A at these twist angles very close to the experimental values are calculated, including $\theta = 9.8°$, $\theta = 17.1°$, $\theta = 20.8°$, $\theta = 23.3°$, and $\theta = 27.5°$ (see Supplemental Material Fig. S19 [56]). The inset shows the relative error $\eta = |(E_A^t/t_0^t) - (E_A^e/t_0^e)|/(E_A^e/t_0^e)$ versus $\theta_\eta = (\theta^e + \theta^t)/2$, where the experimental value of t_0^e in bilayer graphene is measured as 3 eV in Ref. [64] and $t_0^t = 2.8$ eV, with e and t denoting experiment and theory, respectively.

twist-angle-tunable and finite-size-induced optical absorptions from infrared to visible and ultraviolet frequencies allow for promising applications of TBGQDs in photovoltaic devices and photodetectors.

The twist angle dependence of group (i) peaks (called E_A therein) have been experimentally measured in Ref. [47]. In Fig. 9 we compare these experimentally measured E_A with these theoretically obtained values for the triangular TBGQDs with $L \sim 8.03$ nm ($t_0 = 2.8$ eV and $U = 0$ eV). Our results capture the experimental features in an acceptable range with a relative error less than 0.1.

X. CONCLUSION

In conclusion, we derived polarization-dependent optical selection rules for systems with point group symmetries. The changes of the rotational quantum number characterize the selection rules of circularly polarized light. The eigenvalues of symmetry operator $\hat{O}$ (such as the twofold rotational operator or reflection operator) characterize the selection rules of linearly polarized light in D_n, D_{nh}, D_{nd}, and C_{nv} systems. We have designed and classified various TBGQDs into 10 different point group structures which are experimentally feasible and derived an optical selection rule database for all of these quantum dot structures. The calculated current operator matrix elements identify our polarization-dependent selection rules. We analyzed the band gap scaling of TBGQDs and found that it follows a power law with a power index inside $[-2, -1]$ and showed that the twist degree of freedom has a remarkable impact on the size scaling while we found only a weak influence of local Coulomb interactions. We compiled an atlas of both size-dependent and twist-angle-dependent optical spectra of TBGQDs and showed that the optical band gap scaling also follows a power law but with its power indices smaller than those found for the electronic band gap as a result of selection rules. We characterized three groups of optical conductivity peaks in TBGQDs which also appear in infinite twisted bilayer graphene. In addition, we predicted a new group of peaks with multiple discrete absorption frequencies ranging from infrared to ultraviolet energy as a consequence of quantum confinement effects in finite-size TBGQDs. These new peaks render TBGQDs highly promising for applications in photovoltaic devices and photodetectors. Our optical spectrum atlas and derived selection rule database present a comprehensive structure–symmetry-function interrelation and allow an excellent geometrical control of optical properties for TBGQDs as a building block in on-chip carbon optoelectronics [65,66].

ACKNOWLEDGMENTS

S. Y. acknowledges support from the National Science Foundation of China (No. 12174291). H.-Q. L. and Y. W. acknowledge financial support from NSAF (No. U1930402) and NSFC (No. 11734002 and No. 12088101), and computational resources from the Beijing Computational Science Research Center. G. Y. and Y. W. acknowledge support from the China Postdoctoral Science Foundation (Grants No. 2018M632902 and No. 2019M660433) and NSFC (No. 11832019). Y. W. also thanks Dr. Wen Yang at CSRC for fruitful discussions. M. I. K. acknowledges support from the ERC Synergy Grant, Project No. 854843 FASTCORR.

APPENDIX A: PROCEDURES FOR GENERATING TBGQDs

The process involves two steps to generate TBGQDs. Firstly, we define the lattice vectors for each layer and the rotation center between the two layers such that we can construct an infinite twisted bilayer graphene. The atom sites in twisted bilayer graphene are described by

$$\boldsymbol{R}_{l,A(B)} = m_l \boldsymbol{a}_{l,1} + n_l \boldsymbol{a}_{l,2} + \boldsymbol{\tau}_{l,A(B)}, \tag{A1}$$

where layer indices $l = 1, 2$ denote layer 1 and layer 2, respectively, $\boldsymbol{a}_{l,1}$ and $\boldsymbol{a}_{l,2}$ are the basis vectors of each layer, m_l and n_l are arbitrary integers, and $\boldsymbol{\tau}_{l,A(B)}$ is the relative vectors of sublattices A and B inside a unit cell for each layer. For monolayer graphene before twist, if the armchair edge is along the x axis, the basis vectors read

$$\boldsymbol{a}_1 = \frac{\sqrt{3}a}{2}\hat{x} - \frac{a}{2}\hat{y}, \qquad \boldsymbol{a}_2 = \frac{\sqrt{3}a}{2}\hat{x} + \frac{a}{2}\hat{y}. \quad \text{(A2)}$$

If the zigzag edge is along the x axis, the basis vectors read

$$\boldsymbol{a}_1 = a\hat{x} + 0\hat{y}, \qquad \boldsymbol{a}_2 = \frac{a}{2}\hat{x} + \frac{\sqrt{3}a}{2}\hat{y}. \quad \text{(A3)}$$

After a twist between the two monolayers with an angle θ, we can write the basis vectors of layers 1 and 2 as $\boldsymbol{a}_{1,i} = \boldsymbol{R}_{-\theta/2}\cdot\boldsymbol{a}_i$ and $\boldsymbol{a}_{2,i} = \boldsymbol{R}_{\theta/2}\cdot\boldsymbol{a}_i$, with $\boldsymbol{R}_\theta$ as the rotation operation. The rotation geometrical centers can be at atom, hexagon center, or bond center, where their relative vectors of sublattices A and B are respectively given by

$$\boldsymbol{\tau}_{l,A} = \boldsymbol{0}, \qquad \boldsymbol{\tau}_{l,B} = \frac{1}{3}\boldsymbol{a}_{l,1} + \frac{1}{3}\boldsymbol{a}_{l,2}, \quad \text{(A4)}$$

$$\boldsymbol{\tau}_{l,A} = \frac{1}{3}\boldsymbol{a}_{l,1} + \frac{1}{3}\boldsymbol{a}_{l,2}, \qquad \boldsymbol{\tau}_{l,B} = \frac{2}{3}\boldsymbol{a}_{l,1} + \frac{2}{3}\boldsymbol{a}_{l,2}, \quad \text{(A5)}$$

$$\boldsymbol{\tau}_{l,A} = -\frac{1}{6}\boldsymbol{a}_{l,1} - \frac{1}{6}\boldsymbol{a}_{l,2}, \qquad \boldsymbol{\tau}_{l,B} = \frac{1}{6}\boldsymbol{a}_{l,1} + \frac{1}{6}\boldsymbol{a}_{l,2}. \quad \text{(A6)}$$

In the second step, we cut the infinite twisted bilayer graphene into nanoflakes by leaving the atoms only inside a desired polygon and remove the edge atoms with two dangling bonds to reduce defect states. We now show in detail how to choose the rotation geometrical centers and the relative vectors of sublattices to generate TBGQDs with 10 different point group symmetries, respectively.

For structures with point groups D_{nh} and D_n ($n = 2, 3, 6$), the twist angles $\theta = 0$ and $\theta \neq 0$ are required, respectively. For D_{2h} and D_2, we need to cut the infinite bilayers into rectangle nanoflakes with two vertical sides and two horizontal sides. As an example, we have chosen the bond center as the geometrical center with $\boldsymbol{\tau}_{l,A(B)}$ in Eq. (A6) for quantum dots with D_{2h} and D_2, as shown in Figs. 2(a) and 2(b). For $D_{3h}(D_{6h})$ and $D_3(D_6)$, we need to cut the infinite bilayers into triangular (hexagonal) nanoflakes with three (six) sides. The hexagon center is chosen as the geometrical center in quantum dots with D_{3h} in Fig. 2(c), D_3 in Fig. 2(d), D_{6h} in Fig. 2(g), and D_6 in Fig. 2(h).

For structures with point group D_{3d}, the geometrical center is at the C atom with its $\boldsymbol{\tau}_{l,A(B)}$ in Eq. (A4), and the twist angle is zero. The armchair edge is chosen along the x axis with its basis vectors in Eq. (A2). The infinite bilayers are then cut into triangular nanoflakes as shown in Fig. 2(f).

For structures with point groups C_{3v}, C_{6v}, and D_{6d}, the geometrical center is always at the hexagon center with their $\boldsymbol{\tau}_{l,A(B)}$ in Eq. (A5). The bottom and top layers have armchair and zigzag edges along the x axis with their basis vectors in Eqs. (A2) and (A3), respectively. This means that the twist angle θ is 30°. Then, the infinite bilayers are cut into triangular, hexagonal, and dodecagonal nanoflakes for C_{3v}, C_{6v}, and D_{6d}, respectively.

APPENDIX B: HAMILTONIAN

For twisted bilayer graphene systems, the Hubbard Hamiltonian including both the effective tight-binding kinetic energy contributed by the p_z orbital of C atoms and the electron-electron interactions reads

$$H = \sum_{i,s}\varepsilon_i n_{i,s} + \sum_{i,\mathbf{r}_{ij},s} t(\mathbf{r}_{ij}) c^\dagger_{i,s} c_{j,s} + U\sum_i n_{i,\uparrow} n_{i,\downarrow}, \quad \text{(B1)}$$

where $n_{i,s} = c^\dagger_{i,s} c_{i,s}$ with the spin index s, ε_i is the on-site energy and has been set at zero, U is an effective on-site Coulomb repulsion (i.e., U^* [59], here labeled as U for simplicity), and the hopping $t(\mathbf{r}_{ij})$ is written as a function of $\mathbf{r}_{ij}$, i.e.,

$$t(\mathbf{r}_{ij}) = V_{pp\sigma}(|\mathbf{r}_{ij}|)\cos^2\beta + V_{pp\pi}(|\mathbf{r}_{ij}|)\sin^2\beta, \quad \text{(B2)}$$

with $\beta = \hat{z}\cdot\mathbf{r}_{ij}/|\mathbf{r}_{ij}|$. The Slater-Koster bond integrals take the forms as [67]

$$\begin{aligned} V_{pp\sigma}(|\mathbf{r}_{ij}|) &= -t_0 e^{2.218(b_0-|\mathbf{r}_{ij}|)} F(|\mathbf{r}_{ij}|), \\ V_{pp\pi}(|\mathbf{r}_{ij}|) &= t_1 e^{2.218(h-|\mathbf{r}_{ij}|)} F(|\mathbf{r}_{ij}|), \end{aligned} \quad \text{(B3)}$$

where $t_0 = 2.8$ eV, $b_0 = 1.42$ Å, $t_1 = 0.17t_0$ (∼0.48 eV), $F(|\mathbf{r}_{ij}|) = 1/(1 + e^{(|\mathbf{r}_{ij}|-0.265)/5})$, and h is the interlayer distance with 3.35 Å. In our calculations, the cutoff carbon-carbon hopping distance is 5 Å. The p_z-orbital based tight-binding model in Eqs. (B2) and (B3) has been widely used to well describe the electronic structures in twisted bilayer graphene systems [37,41,46,68–71]. The low-energy physics from the p_z-orbital based tight-binding model is also consistent with that from the Wannier-function based tight-binding method [72] and density functional theory [71]. For the correlated sp^2 carbon systems with a moderate local U, the mean-field approximation can successfully capture the low-energy physics occurring in the systems [60,62,63,73]. Within this approximation, the two-body interactions can be decoupled as $n_{i,\uparrow}n_{i,\downarrow} \approx n_{i,\uparrow}\langle n_{i,\downarrow}\rangle + \langle n_{i,\uparrow}\rangle n_{i,\downarrow} - \langle n_{i,\uparrow}\rangle\langle n_{i,\downarrow}\rangle$. With the help of a self-consistent iterative calculation with a high convergence precision of 10^{-6} of $n_{i,s}$, the electronic structure and property of system are determined after minimizing the total energy. We note that the kinetic energy with $t_0 = 2.8$ eV [67,74] is adopted to reproduce the low-energy band structures of untwisted or twisted bilayer graphene systems from *ab initio* calculations [67], and the effective on-site Coulomb interaction $U = 1.2t_0$ [59,60] is used to capture the nonlocal Coulomb interaction [59] at the mean-field level. In our calculations, t_0 is used to measure the Hamiltonian in Eq. (B1) as the energy unit, and the difference results induced by different t_0 in units of eV can be unified by the dimensionless E/t_0 and $\hbar\omega/t_0$.

APPENDIX C: IRREDUCIBLE REPRESENTATIONS

For an eigenstate with its energy E_n and wave function ψ_n^ξ (where $\xi = 1, \ldots, g$, with the degree of degeneracy g), the representation matrix element $D^n_{\xi,\xi'}(\hat{R})$ for an operation class $\hat{R}$ is written as $D^n_{\xi,\xi'}(\hat{R}) = \langle \psi_n^\xi | \hat{R} | \psi_n^{\xi'} \rangle$. The character $\chi^n(\hat{R})$ of the representation of $\hat{R}$ is determined by $\mathrm{Tr}[D^n(\hat{R})]$. We further obtain the reducible representation $\Gamma_{E_n} = \sum_\mu^\oplus a_\mu \Gamma_\mu$ of the energy state E_n by virtue of the number of times Γ_μ, i.e.,

$$a_\mu = \frac{1}{h} \sum_i \chi^n(\hat{R}_i) [\chi^n_{\Gamma_\mu}(\hat{R}_i)]^*, \tag{C1}$$

where h is the order of the point group, and $\hat{R}_i$ is an arbitrary symmetry operation of the system.

APPENDIX D: OPTICAL CONDUCTIVITY

According to the Kubo-Greenwood formula, the real part of interband optical conductivity ($\mathrm{Re}[\sigma_{\alpha\alpha}]$, neglecting the notation Re hereinafter for simplicity) for each spin reads

$$\sigma_{\alpha\alpha}(\omega) = \frac{\pi\hbar}{A} \sum_{mn} \frac{f_m - f_n}{E_n - E_m} \frac{|\langle n|\hat{j}_\alpha|m\rangle|^2 (\gamma/\pi)}{(E_m - E_n - \hbar\omega)^2 + \gamma^2}, \tag{D1}$$

where $A = NA_0$ is the area of quantum dot with $A_0 = 3\sqrt{3}b_0^2/4$ as the average area per atom and N as the number of atoms, $f_m(f_n)$ is the occupation number (Fermi-Dirac distribution function), and the small smearing parameter γ is taken as 0.04 eV in our calculations. The current operator $\hat{j}_\alpha$ is written as

$$\hat{j}_\alpha = e\left(\frac{-i}{\hbar}\right) \sum_{ij} \sum_s (\mathbf{r}_{i,\alpha} - \mathbf{r}_{j,\alpha}) t(\mathbf{r}_{ij}) c^\dagger_{i,s} c_{j,s}, \tag{D2}$$

where s is the spin index. In our calculations, we use the conductivity unit $\sigma_0 = \pi e^2/(4\hbar)$ for the presentation of optical conductivity in a larger range.

On the other hand, the second factor inside the sum term in Eq. (D1) is actually a Dirac δ operator function, which can be expressed as a Fourier transform of the time-evolution operator. In this respect, the real part of optical conductivity can also be written as [75]

$$\sigma_{\alpha\alpha}(\omega) = \lim_{\eta\to 0^+} \frac{e^{-\hbar\omega/k_BT} - 1}{\hbar\omega A} \int_0^\infty e^{-\eta\tau} \sin\omega\tau \times 2\mathrm{Im}\langle\varphi_2(\tau)|\hat{j}_\alpha|\varphi_1(\tau)\rangle_\alpha, \tag{D3}$$

where the wave functions $|\varphi_1(\tau)\rangle_\alpha$ and $|\varphi_2(\tau)\rangle$ take the forms

$$|\varphi_1(\tau)\rangle_\alpha = e^{-iH\tau/\hbar}[1 - f(H)]\hat{j}_\alpha|\varphi_0\rangle,$$
$$|\varphi_2(\tau)\rangle = e^{-iH\tau/\hbar} f(H)|\varphi_0\rangle. \tag{D4}$$

Here, $f(H) = 1/(1 + e^{(H-\mu)/k_BT})$ is a Fermi-Dirac distribution operator with the chemical potential μ, and $|\varphi_0\rangle$ is an initial state consisting of a random superposition of the p_z orbitals at all sites. The time-evolution based calculation in Eq. (D3) is very effective for predicting the optical conductivity of systems with more than tens of thousands of atoms [75], and hence Eq. (D3) is used for periodical systems and large TBGQDs with a lot of atoms. In Supplemental Material Fig. S13 [56], for infinite bilayer graphene our theoretical calculations agree well with the existing results [43] and reproduce twice the universal dynamical conductivity [$\sigma_{\mathrm{mono}} = e^2/(4\hbar)$] of graphene inside the energy range from about $0.3t_0$ to $1.1t_0$ from previous continuum models [76,77]. Note that here our results need to be multiplied by 2π because the used area $A = NA_0$ in our Eqs. (D1) and (D3) is twice the monolayer's area S in previous works [43]. For our calculations the temperature is set at 0 K. We also consider the nonzero temperature and find temperature has only weak influences on the optical conductivity of TBGQDs, as shown in Supplemental Material Fig. S13 [56].

APPENDIX E: STRUCTURE RELAXATION

The atomistic model based on the classical reactive empirical bond order [78] (intralayer interaction) and Kolmogorov-Crespi [79] (interlayer interaction) potentials is implemented in LAMMPS software [80,81]. All of the edge carbon atoms are saturated by hydrogen atoms for the relaxation.

[1] D. H. Goldstein, *Polarized Light* (CRC Press, Boca Raton, FL, 2017).

[2] D. S. Kliger and J. W. Lewis, *Polarized Light in Optics and Spectroscopy* (Elsevier, New York, 2012).

[3] M. Fox, *Quantum Optics: An Introduction* (Oxford University Press, Oxford, England, 2006), Vol. 15.

[4] F. Langer, C. P. Schmid, S. Schlauderer, M. Gmitra, J. Fabian, P. Nagler, C. Schüller, T. Korn, P. Hawkins, J. Steiner *et al.*, *Lightwave Valleytronics in a Monolayer of Tungsten Diselenide*, Nature (London) **557**, 76 (2018).

[5] W. Demtröder, *Atoms, Molecules and Photons* (Springer, New York, 2010), Vol. 3.

[6] E. L. Ivchenko and G. E. Pikus, *New Photogalvanic Effect in Gyrotropic Crystals*, Zh. Eksp. Teor. Fiz. Pis'ma Redaktsiiu **27**, 640 (1978) [JETP Lett. **27**, 604 (1978)], http://jetpletters.ru/ps/1554/article_23792.shtml.

[7] W. Yao, D. Xiao, and Q. Niu, *Valley-Dependent Optoelectronics from Inversion Symmetry Breaking*, Phys. Rev. B **77**, 235406 (2008).

[8] D. Xiao, G.-B. Liu, W. Feng, X. Xu, and W. Yao, *Coupled Spin and Valley Physics in Monolayers of* MoS_2 *and Other*

Group-VI Dichalcogenides, Phys. Rev. Lett. **108**, 196802 (2012).

[9] T. Cao, G. Wang, W. Han, H. Ye, C. Zhu, J. Shi, Q. Niu, P. Tan, E. Wang, B. Liu *et al.*, *Valley-Selective Circular Dichroism of Monolayer Molybdenum Disulphide*, Nat. Commun. **3**, 1 (2012).

[10] K. F. Mak, K. He, J. Shan, and T. F. Heinz, *Control of Valley Polarization in Monolayer* MoS_2 *by Optical Helicity*, Nat. Nanotechnol. **7**, 494 (2012).

[11] H. Zeng, J. Dai, W. Yao, D. Xiao, and X. Cui, *Valley Polarization in* MoS_2 *Monolayers by Optical Pumping*, Nat. Nanotechnol. **7**, 490 (2012).

[12] E. G. Kavousanaki and K. M. Dani, *Optically Induced Magnetic Moments in Symmetric Graphene Quantum Dots*, Phys. Rev. B **91**, 035433 (2015).

[13] A. L. Efros and A. L. Efros, *Interband Absorption of Light in a Semiconductor Sphere*, Sov. Phys. Semicond. **16**, 772 (1982).

[14] L. E. Brus, *Electron-Electron and Electron-Hole Interactions in Small Semiconductor Crystallites: The Size Dependence of the Lowest Excited Electronic State*, J. Chem. Phys. **80**, 4403 (1984).

[15] C. R. Kagan, E. Lifshitz, E. H. Sargent, and D. V. Talapin, *Building Devices from Colloidal Quantum Dots*, Science **353**, aac5523 (2016).

[16] Y.-H. Won, O. Cho, T. Kim, D.-Y. Chung, T. Kim, H. Chung, H. Jang, J. Lee, D. Kim, and E. Jang, *Highly Efficient and Stable* InP/ZnSe/ZnS *Quantum Dot Light-Emitting Diodes*, Nature (London) **575**, 634 (2019).

[17] T. Kim, K.-H. Kim, S. Kim, S.-M. Choi, H. Jang, H.-K. Seo, H. Lee, D.-Y. Chung, and E. Jang, *Efficient and Stable Blue Quantum Dot Light-Emitting Diode*, Nature (London) **586**, 385 (2020).

[18] Z. Liu, C.-H. Lin, B.-R. Hyun, C.-W. Sher, Z. Lv, B. Luo, F. Jiang, T. Wu, C.-H. Ho, H.-C. Kuo *et al.*, *Micro-Light-Emitting Diodes with Quantum Dots in Display Technology*, Light Sci. Appl. **9**, 1 (2020).

[19] J. Shen, Y. Zhu, X. Yang, and C. Li, *Graphene Quantum Dots: Emergent Nanolights for Bioimaging, Sensors, Catalysis and Photovoltaic Devices*, Chem. Commun. **48**, 3686 (2012).

[20] L. Li, G. Wu, G. Yang, J. Peng, J. Zhao, and J.-J. Zhu, *Focusing on Luminescent Graphene Quantum Dots: Current Status and Future Perspectives*, Nanoscale **5**, 4015 (2013).

[21] X. T. Zheng, A. Ananthanarayanan, K. Q. Luo, and P. Chen, *Glowing Graphene Quantum Dots and Carbon Dots: Properties, Syntheses, and Biological Applications*, Small **11**, 1620 (2015).

[22] Z. Zhang, J. Zhang, N. Chen, and L. Qu, *Graphene Quantum Dots: An Emerging Material for Energy-Related Applications and Beyond*, Energy Environ. Sci. **5**, 8869 (2012).

[23] M. Bacon, S. J. Bradley, and T. Nann, *Graphene Quantum Dots*, Part. Part. Syst. Charact. **31**, 415 (2014).

[24] Y. Yan, J. Gong, J. Chen, Z. Zeng, W. Huang, K. Pu, J. Liu, and P. Chen, *Recent Advances on Graphene Quantum Dots: From Chemistry and Physics to Applications*, Adv. Mater. **31**, 1808283 (2019).

[25] S. Zhu, Y. Song, X. Zhao, J. Shao, J. Zhang, and B. Yang, *The Photoluminescence Mechanism in Carbon Dots (Graphene Quantum Dots, Carbon Nanodots, and Polymer Dots): Current State and Future Perspective*, Nano Res. **8**, 355 (2015).

[26] L. A. Ponomarenko, F. Schedin, M. I. Katsnelson, R. Yang, E. W. Hill, K. S. Novoselov, and A. K. Geim, *Chaotic Dirac Billiard in Graphene Quantum Dots*, Science **320**, 356 (2008).

[27] K. A. Ritter and J. W. Lyding, *The Influence of Edge Structure on the Electronic Properties of Graphene Quantum Dots and Nanoribbons*, Nat. Mater. **8**, 235 (2009).

[28] S. Kim, S. W. Hwang, M.-K. Kim, D. Y. Shin, D. H. Shin, C. O. Kim, S. B. Yang, J. H. Park, E. Hwang, S.-H. Choi *et al.*, *Anomalous Behaviors of Visible Luminescence from Graphene Quantum Dots: Interplay between Size and Shape*, ACS Nano **6**, 8203 (2012).

[29] T. Yamamoto, T. Noguchi, and K. Watanabe, *Edge-State Signature in Optical Absorption of Nanographenes: Tight-Binding Method and Time-Dependent Density Functional Theory Calculations*, Phys. Rev. B **74**, 121409(R) (2006).

[30] Z. Z. Zhang, K. Chang, and F. M. Peeters, *Tuning of Energy Levels and Optical Properties of Graphene Quantum Dots*, Phys. Rev. B **77**, 235411 (2008).

[31] T. Basak, H. Chakraborty, and A. Shukla, *Theory of Linear Optical Absorption in Diamond-Shaped Graphene Quantum Dots*, Phys. Rev. B **92**, 205404 (2015).

[32] R. Pohle, E. G. Kavousanaki, K. M. Dani, and N. Shannon, *Symmetry and Optical Selection Rules in Graphene Quantum Dots*, Phys. Rev. B **97**, 115404 (2018).

[33] I. Ozfidan, M. Korkusinski, A. D. Güçlü, J. A. McGuire, and P. Hawrylak, *Microscopic Theory of the Optical Properties of Colloidal Graphene Quantum Dots*, Phys. Rev. B **89**, 085310 (2014).

[34] I. Ozfidan, A. D. Güçlü, M. Korkusinski, and P. Hawrylak, *Theory of Optical Properties of Graphene Quantum Dots*, Phys. Status Solidi RRL **10**, 102 (2016).

[35] J. M. B. Lopes dos Santos, N. M. R. Peres, and A. H. Castro Neto, *Graphene Bilayer with a Twist: Electronic Structure*, Phys. Rev. Lett. **99**, 256802 (2007).

[36] E. Suarez Morell, J. D. Correa, P. Vargas, M. Pacheco, and Z. Barticevic, *Flat Bands in Slightly Twisted Bilayer Graphene: Tight-Binding Calculations*, Phys. Rev. B **82**, 121407(R) (2010).

[37] G. Trambly de Laissardière, D. Mayou, and L. Magaud, *Localization of Dirac Electrons in Rotated Graphene Bilayers*, Nano Lett. **10**, 804 (2010).

[38] R. Bistritzer and A. H. MacDonald, *Moiré Bands in Twisted Double-Layer Graphene*, Proc. Natl. Acad. Sci. U.S.A. **108**, 12233 (2011).

[39] Y. Cao, V. Fatemi, S. Fang, K. Watanabe, T. Taniguchi, E. Kaxiras, and P. Jarillo-Herrero, *Unconventional Superconductivity in Magic-Angle Graphene Superlattices*, Nature (London) **556**, 43 (2018).

[40] B. A. Bernevig, B. Lian, A. Cowsik, F. Xie, N. Regnault, and Z.-D. Song, *Twisted Bilayer Graphene. V. Exact Analytic Many-Body Excitations in Coulomb Hamiltonians: Charge Gap, Goldstone Modes, and Absence of Cooper Pairing*, Phys. Rev. B **103**, 205415 (2021).

[41] S. J. Ahn, P. Moon, T.-H. Kim, H.-W. Kim, H.-C. Shin, E. H. Kim, H. W. Cha, S.-J. Kahng, P. Kim, M. Koshino *et al.*, *Dirac Electrons in a Dodecagonal Graphene Quasicrystal*, Science **361**, 782 (2018).

[42] W. Yao, E. Wang, C. Bao, Y. Zhang, K. Zhang, K. Bao, C. K. Chan, C. Chen, J. Avila, M. C. Asensio *et al.*, *Quasicrystalline 30 Twisted Bilayer Graphene as an Incommensurate Superlattice with Strong Interlayer Coupling*, Proc. Natl. Acad. Sci. U.S.A. **115**, 6928 (2018).

[43] P. Moon and M. Koshino, *Optical Absorption in Twisted Bilayer Graphene*, Phys. Rev. B **87**, 205404 (2013).

[44] H. A. Le and V. N. Do, *Electronic Structure and Optical Properties of Twisted Bilayer Graphene Calculated via Time Evolution of States in Real Space*, Phys. Rev. B **97**, 125136 (2018).

[45] A. Vela, M. V. O. Moutinho, F. J. Culchac, P. Venezuela, and R. B. Capaz, *Electronic Structure and Optical Properties of Twisted Multilayer Graphene*, Phys. Rev. B **98**, 155135 (2018).

[46] G. Yu, Z. Wu, Z. Zhan, M. I. Katsnelson, and S. Yuan, *Dodecagonal Bilayer Graphene Quasicrystal and Its Approximants*, npj Comput. Mater. **5**, 1 (2019).

[47] R. W. Havener, Y. Liang, L. Brown, L. Yang, and J. Park, *van Hove Singularities and Excitonic Effects in the Optical Conductivity of Twisted Bilayer Graphene*, Nano Lett. **14**, 3353 (2014).

[48] N. V. Tepliakov, A. V. Orlov, E. V. Kundelev, and I. D. Rukhlenko, *Twisted Bilayer Graphene Quantum Dots for Chiral Nanophotonics*, J. Phys. Chem. C **124**, 22704 (2020).

[49] T. Westerhout, M. I. Katsnelson, and M. Rösner, *Quantum Dot-like Plasmonic Modes in Twisted Bilayer Graphene Supercells*, 2D Mater. **9**, 014004 (2022).

[50] M. Mirzakhani, F. M. Peeters, and M. Zarenia, *Circular Quantum Dots in Twisted Bilayer Graphene*, Phys. Rev. B **101**, 075413 (2020).

[51] F. Solomon and S. R. Power, *Valley Current Generation Using Biased Bilayer Graphene Dots*, Phys. Rev. B **103**, 235435 (2021).

[52] J. Bucko and F. Herman, *Large Twisting Angles in Bilayer Graphene Moiré Quantum Dot Structures*, Phys. Rev. B **103**, 075116 (2021).

[53] F. A. Cotton, *Chemical Applications of Group Theory* (John Wiley & Sons, New York, 2003).

[54] M. S. Dresselhaus, G. Dresselhaus, and A. Jorio, *Group Theory: Application to the Physics of Condensed Matter* (Springer, New York, 2007).

[55] $\langle\psi_k|\hat{d}_\pm|\psi_l\rangle = e^{(i2\pi/n)(\phi_k-\phi_l)}\langle\psi_k|\hat{C}_n^\dagger\hat{d}_\pm\hat{C}_n|\psi_l\rangle = e^{(i2\pi/n)(\phi_k-\phi_l\pm1)}\langle\psi_k|\hat{d}_\pm|\psi_l\rangle = \delta_{\phi_l,\phi_k\pm1}\langle\psi_k|\hat{d}_\pm|\psi_l\rangle$, where $\hat{d}_\pm = \hat{d}_x \pm i\hat{d}_y$ are the dipole operators for $\sigma^\pm$ polarizations and $\hat{C}_n^\dagger\hat{d}_\pm\hat{C}_n = e^{\pm i2\pi/n}\hat{d}_\pm$ has been used.

[56] See Supplemental Material at http://link.aps.org/supplemental/10.1103/PhysRevX.12.021055 for irreducible representations, symmetry operators, and x axis for the introduced 10 point groups in Table S1, optical conductivity spectra for the other introduced 9 point groups in Figs. S1–S3, current operator matrix elements for the introduced other 7 point groups in Figs. S4–S10, band gap scaling for $u = 1.2t_0$ in Fig. S11 and $u = 0.6t_0$ in Fig. S12, line plots of optical conductivity in Fig. S13, σ_{yy} in Fig. S14, optical conductivity contour plots for $u = 0.6t_0$ in Fig. S15 and $u = 1.2t_0$ in Fig. S16, structure relaxation effects on optical conductivity in Fig. S17, twist angle dependence of optical spectrum for hexagonal quantum dots in Fig. S18, and energy positions of absorption peaks E_A in Fig. S19.

[57] T. Chakraborty, *Quantum Dots: A Survey of the Properties of Artificial Atoms* (Elsevier, New York, 1999).

[58] M. I. Katsnelson, *The Physics of Graphene* (Cambridge University Press, Cambridge, England, 2020).

[59] M. Schüler, M. Rösner, T. O. Wehling, A. I. Lichtenstein, and M. I. Katsnelson, *Optimal Hubbard Models for Materials with Nonlocal Coulomb Interactions: Graphene, Silicene, and Benzene*, Phys. Rev. Lett. **111**, 036601 (2013).

[60] O. V. Yazyev, *Emergence of Magnetism in Graphene Materials and Nanostructures*, Rep. Prog. Phys. **73**, 056501 (2010).

[61] E. H. Hwang and S. Das Sarma, *Dielectric Function, Screening, and Plasmons in Two-Dimensional Graphene*, Phys. Rev. B **75**, 205418 (2007).

[62] A. D. Güçlü, P. Potasz, M. Korkusinski, and P. Hawrylak, *Graphene Quantum Dots* (Springer, New York, 2014).

[63] H. Feldner, Z. Y. Meng, A. Honecker, D. Cabra, S. Wessel, and F. F. Assaad, *Magnetism of Finite Graphene Samples: Mean-Field Theory Compared with Exact Diagonalization and Quantum Monte Carlo Simulations*, Phys. Rev. B **81**, 115416 (2010).

[64] L. M. Zhang, Z. Q. Li, D. N. Basov, M. M. Fogler, Z. Hao, and M. C. Martin, *Determination of the Electronic Structure of Bilayer Graphene from Infrared Spectroscopy*, Phys. Rev. B **78**, 235408 (2008).

[65] D. A. Areshkin and C. T. White, *Building Blocks for Integrated Graphene Circuits*, Nano Lett. **7**, 3253 (2007).

[66] R. B. Payod, D. Grassano, G. N. C. Santos, D. I. Levshov, O. Pulci, and V. A. Saroka, *2N + 4-Rule and an Atlas of Bulk Optical Resonances of Zigzag Graphene Nanoribbons*, Nat. Commun. **11**, 82 (2020).

[67] G. Trambly de Laissardière, D. Mayou, and L. Magaud, *Numerical Studies of Confined States in Rotated Bilayers of Graphene*, Phys. Rev. B **86**, 125413 (2012).

[68] L. Huder, A. Artaud, T. Le Quang, G. T. de Laissardière, A. G. M. Jansen, G. Lapertot, C. Chapelier, and V. T. Renard, *Electronic Spectrum of Twisted Graphene Layers Under Heterostrain*, Phys. Rev. Lett. **120**, 156405 (2018).

[69] A. Kerelsky, L. J. McGilly, D. M. Kennes, L. Xian, M. Yankowitz, S. Chen, K. Watanabe, T. Taniguchi, J. Hone, C. Dean *et al.*, *Maximized Electron Interactions at the Magic Angle in Twisted Bilayer Graphene*, Nature (London) **572**, 95 (2019).

[70] H. Shi, Z. Zhan, Z. Qi, K. Huang, E. van Veen, J. Á. Silva-Guillén, R. Zhang, P. Li, K. Xie, H. Ji *et al.*, *Large-Area, Periodic, and Tunable Intrinsic Pseudo-Magnetic Fields in Low-Angle Twisted Bilayer Graphene*, Nat. Commun. **11**, 1 (2020).

[71] G. Yu, Y. Wang, M. I. Katsnelson, H.-Q. Lin, and S. Yuan, *Interlayer Hybridization in Graphene Quasicrystal and Other Bilayer Graphene Systems*, Phys. Rev. B **105**, 125403 (2022).

[72] S. Fang and E. Kaxiras, *Electronic Structure Theory of Weakly Interacting Bilayers*, Phys. Rev. B **93**, 235153 (2016).
[73] J. Fernández-Rossier and J. J. Palacios, *Magnetism in Graphene Nanoislands*, Phys. Rev. Lett. **99**, 177204 (2007).
[74] A. H. Castro Neto, F. Guinea, N. M. R. Peres, K. S. Novoselov, and A. K. Geim, *The Electronic Properties of Graphene*, Rev. Mod. Phys. **81**, 109 (2009).
[75] S. Yuan, H. De Raedt, and M. I. Katsnelson, *Modeling Electronic Structure and Transport Properties of Graphene with Resonant Scattering Centers*, Phys. Rev. B **82**, 115448 (2010).
[76] C. J. Tabert and E. J. Nicol, *Optical Conductivity of Twisted Bilayer Graphene*, Phys. Rev. B **87**, 121402(R) (2013).
[77] T. Stauber, P. San-Jose, and L. Brey, *Optical Conductivity, Drude Weight and Plasmons in Twisted Graphene Bilayers*, New J. Phys. **15**, 113050 (2013).
[78] D. W. Brenner, O. A. Shenderova, J. A. Harrison, S. J. Stuart, B. Ni, and S. B. Sinnott, *A Second-Generation Reactive Empirical Bond Order (REBO) Potential Energy Expression for Hydrocarbons*, J. Phys. Condens. Matter **14**, 783 (2002).
[79] A. N. Kolmogorov and V. H. Crespi, *Registry-Dependent Interlayer Potential for Graphitic Systems*, Phys. Rev. B **71**, 235415 (2005).
[80] S. Plimpton, *Fast Parallel Algorithms for Short-Range Molecular Dynamics*, J. Comput. Phys. **117**, 1 (1995).
[81] http://lammps.sandia.gov.